biomedicines

MDPI

Article

A Fast, Reliable Oil-In-Water Microemulsion Procedure for Silica Coating of Ferromagnetic Zn Ferrite Nanoparticles Capable of Inducing Cancer Cell Death In Vitro

Stefan Nitica [1,†], Ionel Fizesan [2,†], Roxana Dudric [3], Lucian Barbu-Tudoran [4,5], Anca Pop [2], Felicia Loghin [2], Nicoleta Vedeanu [1], Constantin Mihai Lucaciu [1,*] and Cristian Iacovita [1,*]

[1] Department of Pharmaceutical Physics-Biophysics, Faculty of Pharmacy, "Iuliu Haţieganu" University of Medicine and Pharmacy, 6 Pasteur St., 400349 Cluj-Napoca, Romania; stefan_nitica@yahoo.com (S.N.); nicoletavedeanu@yahoo.com (N.V.)
[2] Department of Toxicology, Faculty of Pharmacy, "Iuliu Haţieganu" University of Medicine and Pharmacy, 6A Pasteur St., 400349 Cluj-Napoca, Romania; ionel.fizesan@umfcluj.ro (I.F.); anca.pop@umfcluj.ro (A.P.); floghin@umfcluj.ro (F.L.)
[3] Faculty of Physics, "Babes-Bolyai" University, Kogalniceanu 1, 400084 Cluj-Napoca, Romania; roxana.dudric@ubbcluj.ro
[4] Electron Microscopy Center "Prof. C. Craciun", Faculty of Biology & Geology, "Babes-Bolyai" University, 5–7 Clinicilor St., 400006 Cluj-Napoca, Romania; lucian.barbu@ubbcluj.ro
[5] Electron Microscopy Integrated Laboratory, National Institute for Research and Development of Isotopic and Molecular Technologies, 67–103 Donath St., 400293 Cluj-Napoca, Romania
* Correspondence: clucaciu@umfcluj.ro (C.M.L.); cristian.iacovita@umfcluj.ro (C.I.); Tel.: +40-744-647-854 (C.M.L.)
† These authors contributed equally to this work.

Citation: Nitica, S.; Fizesan, I.; Dudric, R.; Barbu-Tudoran, L.; Pop, A.; Loghin, F.; Vedeanu, N.; Lucaciu, C.M.; Iacovita, C. A Fast, Reliable Oil-In-Water Microemulsion Procedure for Silica Coating of Ferromagnetic Zn Ferrite Nanoparticles Capable of Inducing Cancer Cell Death In Vitro. *Biomedicines* **2022**, *10*, 1647. https://doi.org/10.3390/biomedicines10071647

Academic Editor: Anna Herman-Antosiewicz

Received: 30 May 2022
Accepted: 6 July 2022
Published: 8 July 2022

Abstract: The applications of ferrimagnetic nanoparticles (F-MNPs) in magnetic hyperthermia (MH) are restricted by their stabilization in microscale aggregates due to magnetostatic interactions significantly reducing their heating performances. Coating the F-MNPs in a silica layer is expected to significantly reduce the magnetostatic interactions, thereby increasing their heating ability. A new fast, facile, and eco-friendly oil-in-water microemulsion-based method was used for coating $Zn_{0.4}Fe_{2.6}O_4$ F-MNPs in a silica layer within 30 min by using ultrasounds. The silica-coated clusters were characterized by various physicochemical techniques and MH, while cytotoxicity studies, cellular uptake determination, and in vitro MH experiments were performed on normal and malignant cell lines. The average hydrodynamic diameter of silica-coated clusters was approximately 145 nm, displaying a high heating performance (up to 2600 W/g_{Fe}). Biocompatibility up to 250 $\mu g/cm^2$ (0.8 mg/mL) was recorded by Alamar Blue and Neutral Red assays. The silica-coating increases the cellular uptake of $Zn_{0.4}Fe_{2.6}O_4$ clusters up to three times and significantly improves their intracellular MH performances. A 90% drop in cellular viability was recorded after 30 min of MH treatment (20 kA/m, 355 kHz) for a dosage level of 62.5 $\mu g/cm^2$ (0.2 mg/mL), while normal cells were more resilient to MH treatment.

Keywords: zinc ferrite nanoparticles; silica coating; oil-in-water microemulsion; ultrasonication; magnetic hyperthermia; cancer cells; A549 cells; BJ cells; Alamar Blue; Neutral Red

1. Introduction

In the field of novel cancer therapy, magnetic nanoparticles (MNPs) are widely investigated within magnetic hyperthermia (MH) treatment [1–3]. The technique exploits the Néel magnetic relaxation, Brownian rotation, and hysteresis losses of MNPs, when subjected to an alternating magnetic field (AFM), to generate sufficient heat for inducing cancer cell death [4–6]. Ferri- or ferromagnetic nanoparticles (F-MNPs) are most desirable for MH applications since their heating capabilities are one order of magnitude greater in comparison with superparamagnetic iron oxide nanoparticles (SPIONs), due to the increase

in both their size and dynamic hysteresis area [7–9]. However, the F-MNPs present a great disadvantage for in vivo and in vitro MH applications as they possess poor colloidal stability in biological media. The permanent magnetic moments of F-MNPs give rise to magnetostatic interactions among them that hinder their dispersion in biological media and favor their stabilization in microscale aggregates [10,11]. The magnetostatic interactions among F-MNPs depend on the distances between them, therefore these interactions may be reduced by introducing a non-magnetic coating around F-NPMag [12,13].

One of the most used methods for the surface modification of MNPs is silica coating [14]. The silica layer around F-MNPs avoids their interaction and agglomeration, providing colloidal stability and keeping them as effective magneto-mechanical actuators required for MH applications [15–19]. On the other hand, the intrinsic toxicity of MNPs is significantly reduced under the protection of silica shells, which have been demonstrated to be nontoxic and biocompatible for biomedical research [20–24]. The silica shells are visible and transparent to near-infrared, and the ultraviolet regions do not interfere with magnetic fields, allowing the MNPs to keep their original magnetic properties [25–29]. Moreover, the silica chemistry facilitates the easy attachment of functional molecules—especially those bearing amine of carboxyl groups—thus adding new functionalities to the hybrid nanostructures, such as fluorescence [29–31] and therapeutic [31–33] and catalytic functions [34]. As it was recently demonstrated, the attachment of a chemotherapeutic agent to the MNPs, reduced the cytotoxic effect of the drug in non-cancerous cells, improved the internalization in cancer cells, and its activity was synergistically enhanced in combination with magnetic hyperthermia [35]. Thus, the controlled encapsulation of the MNPs in a silica shell, by preserving their magnetic properties, enhancing their biocompatibility, and increasing their ability for functionalization with various functional groups represents a huge potential for future clinical translation of the MH technique.

The encapsulation of pre-synthesized MNPs in a SiO_2 layer was usually performed through the hydrolysis of tetraethyl orthosilicate (TEOS) by an aqueous solution of ammonia -$NH_{3(aq)}$ and the subsequent condensation of silica precursors on the surface of the MNPs. A well-known procedure is based on heterogeneous mixtures of water and an organic solvent (usually cyclohexane) formed and stabilized with the help of a surfactant (a widely used one is polyoxyethylene nonyl phenyl ether-Igepal CO-520) called water-in-oil (w/o) microemulsions. The nanometer-sized water droplets dispersed in the organic solvent act as nanoreactors capable of forming a SiO_2 layer around MNPs under a mechanical stirring over at least 12 h [19–21,23,26,27,30,31,34,36–40]. This method was mainly applied to $SPION_S$, and it allowed the formation of a homogeneous SiO_2 layer and fine control of its thickness, around individual SPIONs. Recently, our research group succeeded in encapsulating polyhedral F-NPMag clusters following the w/o microemulsion method [41]. Another commonly used method for encapsulating MNPs in a SiO_2 layer was based on the Stöber process in a sol-gel approach in which the organic solvent was replaced by ethanol or propanol [15–18,22,24,25,29,33,42–44]. This method requires an additional step in which the pre-synthesized MNPs are coated with a polymer, usually polyvinylpyrrolidone (PVP), to make their encapsulation in the SiO_2 layer more efficient.

The main disadvantage of both methods is the very long duration (from a few hours to a few days) necessary to form the SiO_2 layer around MNPs. The use of SiO_2-coated MNPs in both in vitro and in vivo studies, and later in clinical trials, requires large quantities of MNPs@SiO_2, the preparation of which can last even weeks/months due to the long duration of the synthetic procedure. Therefore, the elaboration of a procedure by which the SiO_2 coating of any type of MNPs can be achieved as quickly and efficiently as possible is a major purpose in this field. Moreover, in the case of F-MNPs, the encapsulation procedure must also inhibit the formation of large (micrometric) aggregates before the growth of the SiO_2 layer around the pre-existing F-MNPs clusters following the synthesis method.

Herein, we report the coating of ferromagnetic zinc (Zn) doped iron oxide nanoparticles with an SiO_2 layer by using oil-in-water (o/w) microemulsions, which eliminates the need for the expensive surfactant Igepal CO-520 and for large volumes of organic solvent

(cyclohexane) in the synthesis process, shortening the overall time frame to a maximum of 30 min. The magnetic cores and the coatings were fully characterized using multiple analytical methods such as transmission electron microscopy (TEM), infrared spectroscopy (FT-IR), X-ray diffraction (XRD), and dynamic light scattering (DLS). Further, the magnetic and the heating properties were analyzed by a vibrating sample magnetometer (VSM) and a magnetic hyperthermia (MH) system. The biological assessment included cytotoxicity and cellular uptake determination in cancerous and normal cell lines. Finally, we demonstrated the potential of the silica-coated clusters to induce cell death in vitro.

2. Materials and Methods

2.1. Synthesis of MNPs

The Zn ferrites were synthesized through thermal decomposition of a mixture of metal acetylacetonates with surfactants in a high-boiling point organic solvent. Briefly, iron (III) acetylacetonate (1.5 mmol) (Merck Schuchardt OHG, Hohenbrunn, Germany), zinc (II) acetylacetonate (2.25 mmol) (Merck KGaA, Darmstadt, Germany), oleic acid (3.8 mmol) (Sigma-Aldrich, Steinheim, Germany), and 10 mL benzyl ether (Sigma-Aldrich, Steinheim, Germany) were mixed and magnetically stirred under a flow of nitrogen. The mixture was placed in a 50 mL three-neck, round-bottom flask and heated to 300 °C, at a ramping rate of 5 °C/min, under a continuous flow of nitrogen. The mixture was kept at reflux for 30 min and then cooled down to room temperature by removing the heat source. The Zn ferrites were separated by a neodymium magnet and washed in a mixture of hexane (Honeywell, Seelze, Germany)–ethanol (Chemical, Iasi, Romania) (1:1, v/v) five times. Finally, the as-synthesized Zn ferrites were dispersed in a volume of hexane at a concentration of 10 mg_{MNPs}/mL and stored in a glass container.

2.2. Silica Coating of MNPs

The silica shell was coated on the hydrophobic Zn ferrites via the microemulsion method. First, we tested the water-in-oil emulsion method, which was previously reported in the literature. We tried to improve this method by using ultrasounds for reducing the preparation time. Afterward, because the size of the clusters was too large, we tested a new method based on the oil-in-water emulsion. The emulsions were prepared in 100 mL glass bottles with a thread and a cap, using the following recipes:

a. Classical water-in-oil microemulsion procedure: Briefly, 18 mL cyclohexane (Sigma-Aldrich, Steinheim, Germany) and 1.2 mL Igepal CO-520 (Sigma-Aldrich, Steinheim, Germany) were mixed for 30 min. Afterward, 4 mg of $Zn_{0.4}Fe_{2.6}O_4$ dispersed in 2 mL cyclohexane were added, while stirring. After 5 min, 0.05 mL APTES (Sigma-Aldrich, Steinheim, Germany) and 0.1 mL TEOS (Sigma-Aldrich, Steinheim, Germany) were added, followed by 0.15 mL aqueous ammonia solution (25%). The dispersions were stirred at room temperature for 24 h.
b. Ultrasound assisted water-in-oil microemulsion procedure: Briefly, 18 mL cyclohexane, 1.2 mL Igepal CO-520, 0.4 mL colloidal suspension in hexane (containing 4 mg of $Zn_{0.4}Fe_{2.6}O_4$ NPs), 0.1 mL TEOS, and 0.05 mL APTES were mixed for 30 min, following the addition of 0.5 mL 25% aqueous ammonia solution and 1.5 mL ultrapure water. The mixture was subjected to ultrasonication for 30 min in a water bath sonicator Elmasonic S 30 (Elma Schmidbauer GmbH, Singen, Germany) operating at 37 kHz, with an effective acoustic power of 80 W in continuous mode.
c. Ultrasound-assisted oil-in-water microemulsion procedure: Briefly, 18 mL of ultrapure water, 0.8 mL of TWEEN 20 (Sigma-Aldrich, Steinheim, Germany), 4 mg of Zn ferrites dispersed in 0.4 mL of hexane, and 0.1 mL of TEOS were introduced in a bottle with cap. The mixture was mixed for 5 min by alternating ultrasonication with short cycles (approx. 5 s) of manual stirring, after which 2 mL of 25% (m/v) aqueous ammonia solution was added, and the mixture was subjected to ultrasonication for 30 min. In the last 3 min of sonication, the bottle cap was removed to facilitate the

evaporation of the solvent from the fine droplets and the complete encapsulation of the remaining MNPs.

The mixtures were further treated with an equal volume of ethanol and the silica-coated Zn ferrites were separated by a neodymium magnet. The $Zn_{0.4}Fe_{2.6}O_4$@SiO_2 were furthermore washed in ethanol once and in water three times before being redispersed in water (2 mg MNPs core per mL of water) for storage.

2.3. Characterization Methods

The morphology and the chemical composition of nanostructures were studied by transmission electron microscopy (TEM), using a Hitachi HD2700 (Hitachi, Tokyo, Japan) microscope operating at 200 kV and coupled with an EDX (energy-dispersive X-ray) detector (Oxford Instruments, Oxford, UK, AZtec Software, version 3.3), employing carbon-coated copper grids. Powder X-ray diffraction (XRD) measurements were performed with a Bruker D8 Advance diffractometer using Cu Kα radiation (Bruker AXS GmbH, Karlsruhe, Germany). Fourier transform infrared (FT-IR) spectra were recorded on a TENSOR II instrument (Bruker Optics Inc., Billerica, MA, USA) in attenuated total reflectance mode, using the platinum attenuated total reflectance (ATR) accessory with a single reflection diamond ATR. The spectra were recorded with a resolution of 4 cm^{-1} and 16 scans per sample between 400 and 4000 cm^{-1}. Particle solutions with a concentration of 10 $\mu g_{MNPs}/mL$ were employed to determine the hydrodynamic size and zeta potential using a Zetasizer Nano *ZS*90 (Malvern Instruments, Worcestershire, UK) operating at room temperature in a 90° configuration. Magnetization measurements were carried out using a Cryogenic Limited (London, UK) vibrating sample magnetometer (VSM) under applied magnetic fields from 0 to $\pm$4 T at both 4 K and 300 K. The heating efficiency was evaluated using a commercially available magnetic hyperthermia system, the Easy Heat 0224 from Ambrell (Scottsville, NY, USA) equipped with an optical fiber temperature sensor (0.1 °C accuracy). A volume of 0.5 mL of MNPs was placed in the center of an 8-turn coil using a thermally isolated Teflon holder and then submitted to an AC magnetic field with fixed frequency (355 kHz) and variable amplitude (5–65 kA/m). Details of specific absorption rate (SAR) calculations are provided in the Supplementary Materials (Section S1).

2.4. Cell Lines

For in vitro studies, a human pulmonary carcinoma A549 cell line and a human foreskin fibroblast BJ cell line were purchased from American Type Culture Collection (ATCC, Manassas, VA, USA) and used. Cells were maintained in Dulbecco's Modified Eagle Medium (DMEM, Gibco, Paisley, UK) supplemented with 10% Fetal Bovine Serum (FBS, Gibco, Paisley, UK) at a temperature of 37 °C and 5% CO_2 supplementation. Media was changed every other day, and the cellular cultures were either sub-cultured or used in the experiments at a confluency of 80–90%.

2.5. In Vitro Cytocompatibility Assays

Alamar Blue (AB) and Neutral Red (NR) assays were used to evaluate the cytotoxicity upon a 24 h exposure of the two cell lines to both $Zn_{0.4}Fe_{2.6}O_4$@SiO_2 and $Zn_{0.4}Fe_{2.6}O_4$ NPs. Both types of cells were seeded in 6-well plates for 24 h, following 24 h exposure to NPs suspension at reached doses of 16, 31, 62.5, 125, and 250 $\mu g/cm^2$. The AB and the NR dyes were then added upon thoroughly washing the cells with PBS. A volume of 200 μM resazurin solution was added; and, cells were incubated for 3 h, while the fluorescence was measured at an $\lambda_{excitation}$ = 530/25 nm and $\lambda_{emission}$ = 590/35 nm for the AB assay. A filtered NR dye solution (40 $\mu g/mL$) was used to incubate cells for 2 h, following a washing step to remove the non-internalized dye for NR assay. A 50% hydroalcoholic solution containing 1% glacial acetic acid was further employed to solubilize the intracellular accumulated dye, while the fluorescence was measured at a $\lambda_{excitation}$ = 530/25 nm and a $\lambda_{emission}$ = 620/40 nm. A Synergy 2 Multi-Mode Microplate Reader was used for fluorescence measurements that were realized in biological triplicates.

2.6. Evaluation of Cellular Uptake

The cellular uptake of both $Zn_{0.4}Fe_{2.6}O_4$@SiO_2 and $Zn_{0.4}Fe_{2.6}O_4$ NPs was evaluated upon 24 h incubation. Qualitative evaluation was performed using Prussian Blue staining: cells were fixed with 4% paraformaldehyde for 30 min, and stained with a mixture containing a 2% HCl and a 2% potassium ferrocyanide aqueous solutions; after the development of the blue color, cells were washed three times with PBS, counterstained with Eosin, and finally visualized under a light microscope at a magnification of 100×. For quantitative determinations, the cells were washed, trypsinized, centrifuged for 5 min at 4500× *g*, and then processed for the Fe^{3+} quantification using the Liebig reaction of free Fe^{3+} with thiocyanate, as described in the Supplementary Materials (Section S2).

2.7. In Vitro Magnetic Hyperthermia

A549 and BJ cells were seeded in 6-well plates for 24 h and then further exposed for an additional 24 h to $Zn_{0.4}Fe_{2.6}O_4$@SiO_2 NPs to reach the following concentrations: 31, 62.5, and 125 μg/cm^2. After the exposure, cells were thoroughly washed with PBS, detached using 300 μL of trypsin (0.05%) and then further neutralized with 2700 μL media containing FBS. The cellular suspension was equally divided into two aliquots, centrifuged for 10 min at 100× *g*, and 1300 μL of supernatant was removed from both aliquots. One of the aliquots was kept in a water bath at 37 °C (negative control), while the other aliquot was exposed to an alternating magnetic field (AMF) for 30 min, working at a fixed frequency of 355 kHz and amplitudes of 15, 20, and 30 kA/m. The cells were placed in an Eppendorf tube in the middle of an 8-turn coil. The tube was surrounded by plastic pipes connected to a Peltier element and thermostated at 37 °C. After the AMF exposure, cells from exposed and unexposed aliquots were plated in 96-wells as 6 technical replicates, and cellular viability was measured using the AB and the NR assays after 24 h. Each experiment was performed in three biological replicates. Data were normalized to the AMF negative control (cells exposed to $Zn_{0.4}Fe_{2.6}O_4$@SiO_2 NPs but not to the AMF).

2.8. Statistics

The data are presented as average values ± standard deviation (SD). Data sets were analyzed using a One-way Analysis of Variance (ANOVA) with a post-hoc + Dunn's test, and the graphical representations were done in SigmaPlot 11.0 computer software (Systat). Statistical results showing p values < 0.05 were considered statistically significant.

3. Results and Discussion

3.1. Magnetic Nanoparticles Characterization

It is well known that non-stoichiometric Zn ferrite NPs ($Zn_xFe_{3-x}O_4$), with a Zn content in the range $0.3 < x < 0.5$ and exhibiting a cubic shape represent very efficient nano heaters for magnetic hyperthermia. For that reason, this class of MNPs was chosen as the magnetic core for this study. The Zn ferrite NPs have been synthesized following the thermal decomposition method elaborated by Noh et al. [45]. As revealed by TEM (Figure 1a), the obtained Zn ferrite NPs have a mean edge length of 28 ± 2 nm, and they are approximatively cubic-like in shape. The Fe and the Zn elements are homogeneously distributed within the total volume of the MNPs, as shown by energy-dispersive X-ray (EDX) maps of Fe, Zn, and O elements in the Zn ferrite NPs (Figure 1b). No core/shell structures of MNPs containing only Fe or Zn were observed. The quantitative analysis of the EDX spectra recorded over many MNPs provides a mean value of the Zn atomic percentage (x) of approximately 0.4, resulting from the Zn doped iron oxide NPs with the formula $Zn_{0.4}Fe_{2.6}O_4$. The XRD pattern (Figure 1c) of uncoated $Zn_{0.4}Fe_{2.6}O_4$ NPs corresponds to the cubic spinel crystal structure of magnetite. All the characteristic diffraction peaks are slightly shifted to lower 2 θ angles due to the incorporated Zn ions. Furthermore, no peaks related to ZnO are detected, indicating the successful incorporation of Zn into the magnetite lattice and the formation of spinel $Zn_{0.4}Fe_{2.6}O_4$. The corresponding lattice parameter was found to be a = 0.8410(4) nm, significantly higher than that of magnetite (a = 0.8396 nm), indicating that

the Zn ions occupy the tetrahedral sites. The average crystalline size (27 nm), calculated using Scherrer's formula by Gaussian fit of the peaks (220), (311), and (440), matches the average edge length obtained from TEM images, suggesting that most of $Zn_{0.4}Fe_{2.6}O_4$ are single crystals. The magnetic characterization of the uncoated $Zn_{0.4}Fe_{2.6}O_4$ MNPs revealed the preferential incorporation of Zn ions at the tetrahedral sites, thus leading to a significant increase in the saturation magnetization (M_s) to 100 emu/g with respect to that of bulk magnetite (90 emu/g), as indicated by the low temperature (4 K) hysteresis loop (Figure 1d). The M_s decreases to 72 emu/g at room temperature, which is consistent with the literature [23,28,46,47], and it can be attributed to increased spin-disorders in the surface layers of smaller MNPs [48]. The ferrimagnetic character of $Zn_{0.4}Fe_{2.6}O_4$ is preserved at room temperature, as can be seen from the inset of Figure 1d; the coercive field (H_c) slightly decreases from 29 mT (24 kA/m) to 19 mT (15 kA/m) by increasing the temperature from 4 to 300 K. Upon water transfer through the oxidation of oleic acid by sodium periodate, the $Zn_{0.4}Fe_{2.6}O_4$ acquired a zeta potential of −52 mV due to the resulted carboxyl groups [49], indicating good colloidal stability. However, according to DLS data, the ferrimagnetic $Zn_{0.4}Fe_{2.6}O_4$ NPs have a mean hydrodynamic diameter of 70 nm in water, signifying that they stabilize in an aqueous solution in very small clusters, comprising only a few NPs (Figure 1e).

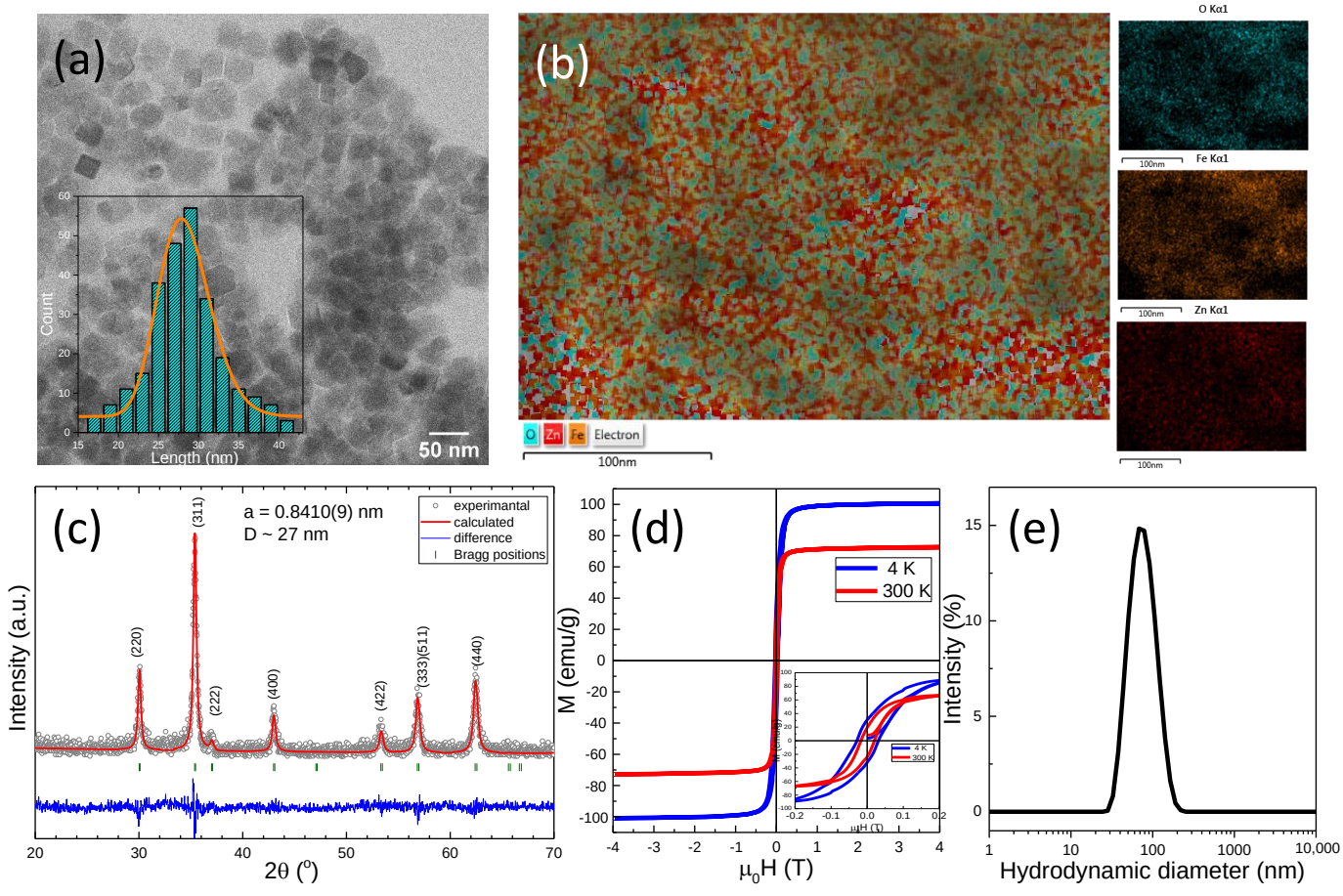

Figure 1. (**a**) TEM images of $Zn_{0.4}Fe_{2.6}O_4$ NPs. Inset represents the size distribution histogram of $Zn_{0.4}Fe_{2.6}O_4$ NPs fitted to a log-normal distribution (orange line). (**b**) EDX global chemical map together with chemical maps of Fe, Zn, and O elements of $Zn_{0.4}Fe_{2.6}O_4$ NPs. (**c**) XRD diffraction pattern of $Zn_{0.4}Fe_{2.6}O_4$ NPs. (**d**) Hysteresis loops of $Zn_{0.4}Fe_{2.6}O_4$ NPs acquired at 4 K and 300 K. Inset represents the low-field regime of hysteresis loops. (**e**) Hydrodynamic diameter resulted from DLS measurements of $Zn_{0.4}Fe_{2.6}O_4$ NPs dispersed in water at a concentration of 10 μg_{MNPs}/mL.

3.2. Silica Coating of Magnetic Nanoparticles

The classical coating method consisting of mechanical stirring over 24 h of a *w/o* (reverse) microemulsion has been firstly applied to encapsulate the hydrophobic $Zn_{0.4}Fe_{2.6}O_4$ clusters in a silica shell. This sample also represents a reference for the present study. As seen in the TEM images of Figure 2a,b, clusters of several tens of MNPs are encapsulated in a thin silica shell and denoted $Zn_{0.4}Fe_{2.6}O_4$@SiO_2-W. The mean hydrodynamic diameter of the resulted $Zn_{0.4}Fe_{2.6}O_4$@SiO_2 clusters increased considerably to 400 nm with respect to that of uncoated $Zn_{0.4}Fe_{2.6}O_4$ NPs (Figure 2e). As evidenced by FT-IR spectroscopy, the absorption band originated from the Fe-O bond dominates the spectra, and it is slightly deviated to 566 cm^{-1} (compared to 549 cm^{-1} for uncoated $Zn_{0.4}Fe_{2.6}O_4$) due to the attachment of SiO_2 to the NP's surface (Figure 2f). The wide absorption band located at 1039 cm^{-1}, due to the stretching vibration of the Si-O-Si bond, proves the presence of the thin layer of SiO_2 around the $Zn_{0.4}Fe_{2.6}O_4$ clusters (red curve in Figure 2f) [37].

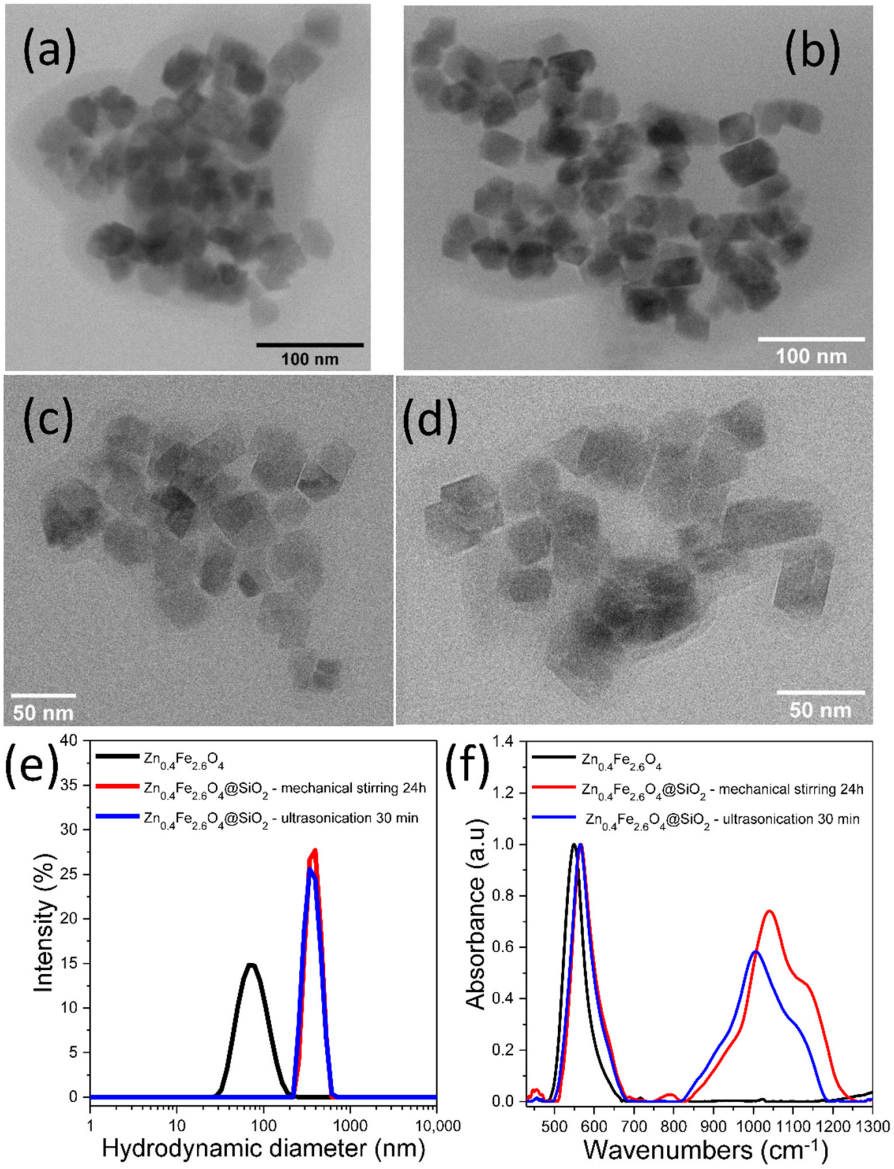

Figure 2. TEM images of $Zn_{0.4}Fe_{2.6}O_4$@SiO_2-W clusters made via *w/o* microemulsion using (**a**,**b**) mechanical stirring for 24 h and (**c**,**d**) ultrasonication for 30 min. (**e**) Hydrodynamic diameter resulted from DLS measurements of uncoated $Zn_{0.4}Fe_{2.6}O_4$ and $Zn_{0.4}Fe_{2.6}O_4$@SiO_2-W clusters dispersed in water at a concentration of 10 μg_{MNPs}/mL. (**f**) FT-IR spectra of uncoated $Zn_{0.4}Fe_{2.6}O_4$ and $Zn_{0.4}Fe_{2.6}O_4$@SiO_2-W clusters. The spectra are normalized to the highest absorption band.

In the second phase of our study, the mechanical stirring of the *w/o* microemulsion was replaced by ultrasonication [50]. The experiments revealed that 30 min ultrasonication of the same reaction composition resulted in the formation of a silica layer around $Zn_{0.4}Fe_{2.6}O_4$ clusters (Figure 2c,d). The $Zn_{0.4}Fe_{2.6}O_4$@SiO_2-W clusters displayed a similar mean hydrodynamic diameter as those formed by mechanical stirring (Figure 2e). The silica layer is slightly thinner as evidenced by the deviation of the Fe-O bond absorption band to 564 cm^{-1} and the occurrence of a less intense Si-O-Si bond absorption band located at 1005 cm^{-1} (blue curve in Figure 2f). Therefore, the ultrasonication considerably reduces the actual formation time of the SiO_2 layer around $Zn_{0.4}Fe_{2.6}O_4$ clusters through the *w/o* microemulsion method from 24 h to 30 min. It has to be mentioned that mechanical stirring allows SPIONs to remain colloidally distributed throughout the mixture volume during the entire silanization process, but in the case of larger or F-MNPs stabilized in clusters, there is a risk of sedimentation. The high energy supplied to the mixture by ultrasounds led primarily to fine emulsification of the internal phase. In other words, very small water droplets were formed, producing a significant increase in the surface area available for the hydrolysis of SiO_2 precursors at the interface between the two phases. At the same time, the colloidal stability of the dispersion was maintained, and when F-MNPs are used, the ultrasounds prevented their agglomeration. The ultrasounds also increased the number of collisions between $Zn_{0.4}Fe_{2.6}O_4$ clusters, dispersed in the external phase of the mixture, and the water droplets containing ammonia (internal phase of the mixture). Simultaneously with these three actions, the energy released by ultrasounds accelerated the hydrolysis of SiO_2 precursors at the interface between the two phases, leading to the formation of the SiO_2 layer within 30 min.

The significant reduction of the silica coating time to 30 min facilitates the preparation in a short time of large quantities necessary for both in vivo and in vitro evaluation. However, the high average hydrodynamic diameter of $Zn_{0.4}Fe_{2.6}O_4$@SiO_2-W clusters of 400 nm might represent a disadvantage for such studies. To decrease the average hydrodynamic diameter of $Zn_{0.4}Fe_{2.6}O_4$@SiO_2-W clusters, different strategies within *w/o* microemulsion, consisting of variations in the concentration of internal phase (water droplets) and external phase (MNPs, IGEPAL-CO520, ammonia, or TEOS) have been applied. Unfortunately, all attempts to obtain smaller clusters failed, the only positive result achieved was the control over the SiO_2 layer thickness of $Zn_{0.4}Fe_{2.6}O_4$@SiO_2-W clusters. In this regard, the *w/o* microemulsion has been replaced with an o/w microemulsion. In this case, the internal phase consists of droplets containing hydrophobic $Zn_{0.4}Fe_{2.6}O_4$ NPs dispersed in hexane, and TWEEN 20 was used as the surfactant. By ultrasonication, these droplets become very small and disperse into the entire volume of the external phase, which is a diluted aqueous solution of ammonia. These very small droplets, containing hydrophobic $Zn_{0.4}Fe_{2.6}O_4$ NPs, practically inhibit their agglomeration into micrometric aggregates, thus offering the possibility to encapsulate the nanometric size clusters of $Zn_{0.4}Fe_{2\cdot.6}O_4$ NPs confined in droplets in an SiO_2 layer (Figure 3a,b) by the rapid hydrolysis of TEOS at the interface of the two phases under the action hydroxide ions generated by ammonia. According to the DLS measurements, the average hydrodynamic diameter of $Zn_{0.4}Fe_{2.6}O_4$@SiO_2-O clusters is approximately 145 nm (Figure 3c). As can be seen in TEM images (Figure 3a,b), the resulted SiO_2 layer is thicker as compared to the previous two samples (Figure 2a–d). In this case, the FTIR spectrum is dominated by the absorption bands characteristic of the SiO_2 layer (red curve in Figure 3d): the stretching vibration band of the Si-O-Si bond located at 1060 cm^{-1} is the most intense, followed by the bending vibration band of Si-O-Si bond (455 cm^{-1}) and the stretching vibration band of the Si-O bond (791 cm^{-1}). The shoulder at 965 cm^{-1} is attributed to Si-OH vibrations (Figure 3d). The less intensive absorption band corresponds to the Fe-O bond being noticeable deviated to 573 cm^{-1}, as compared to the uncoated sample (Figure 3d).

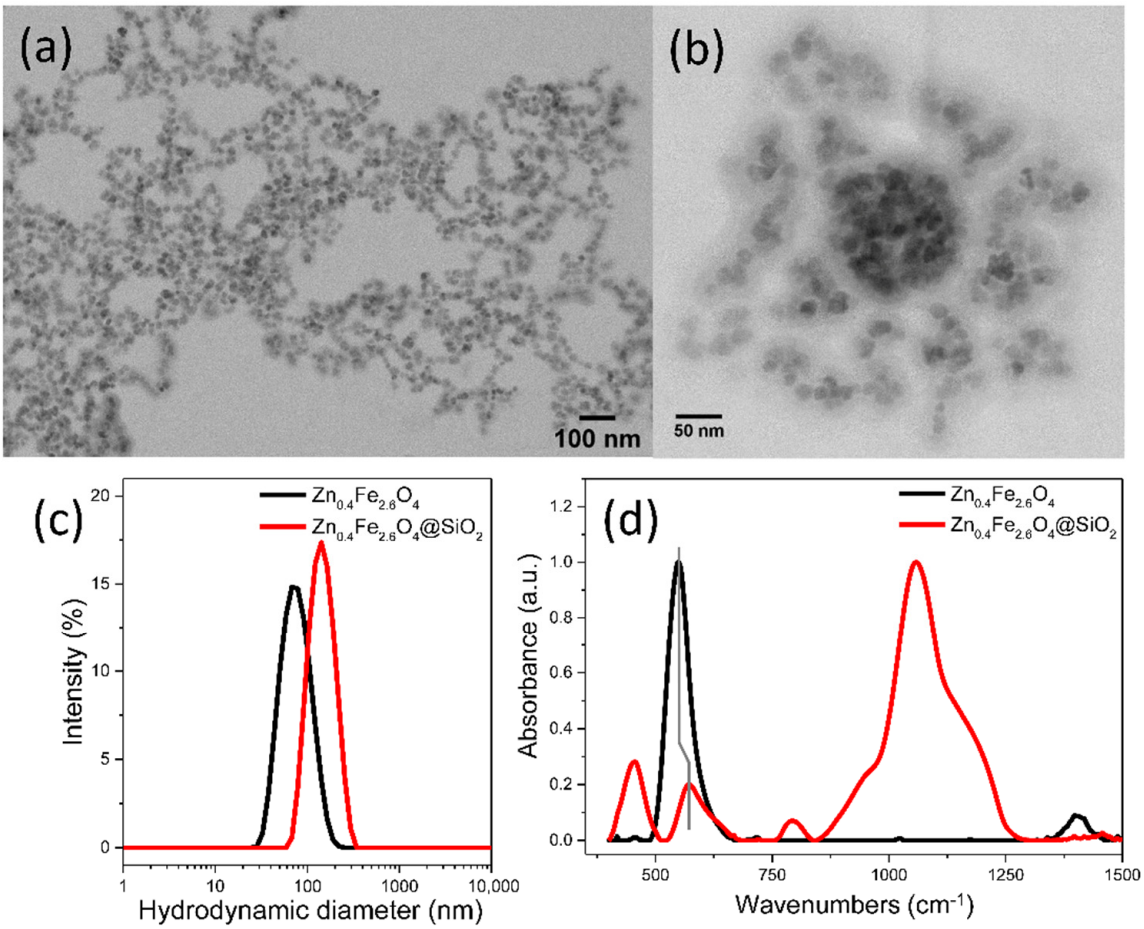

Figure 3. (**a**) Large scale and (**b**) zoom-in TEM images of $Zn_{0.4}Fe_{2.6}O_4$@SiO_2-O clusters. (**c**) Hydrodynamic diameter resulted from DLS measurements of $Zn_{0.4}Fe_{2.6}O_4$ and $Zn_{0.4}Fe_{2.6}O_4$@SiO_2-O clusters dispersed in water at a concentration of 10 μg_{MNPs}/mL. (**d**) FT-IR spectra of $Zn_{0.4}Fe_{2.6}O_4$ and $Zn_{0.4}Fe_{2.6}O_4$@SiO_2-O clusters. The spectra are normalized to the highest absorption band.

3.3. Magnetic Hyperthermia Capabilities

The Specific Absorption Rate (SAR) values of $Zn_{0.4}Fe_{2.6}O_4$@SiO_2 clusters, formed by *w*/*o* and *o*/*w* microemulsion using the ultrasounds and dispersed either in water or PEG8K, obtained by calorimetric measurements (Figures S1–S3), were measured as a function of the amplitude (H) of the applied alternating magnetic field (AMF) at a fixed frequency (355 kHz), as shown in Figure 4. The SAR evolution with H presents a sigmoidal shape, which is characteristic of F-MNPs with a nonzero hysteresis at the measuring temperature. In the absence of any analytical expression, the SAR evolution with H can be fitted using a simple logistic function (Section S1). This type of function allows the calculation of the most important parameters for characterizing the heating performances of MNPs such as the SAR_{max} (the saturation value of SAR), the H_{chyp} (the hyperthermia coercive field, and the point of maximum slope in the SAR = f(H) function). At a concentration of 1 mg_{Fe}/mL, the SAR values of uncoated $Zn_{0.4}Fe_{2.6}O_4$ clusters are 20 and 105 W/g_{Fe} for 5 and 10 kA/m, respectively. For H of 15 kA/m, which represents the H_c at room temperature, the SAR increases four times up to 535 W/g_{Fe}, and it continues to rise to 3120 W/g_{Fe} for 35 kA/m. By further increasing the H (40–65 kA/m), the SAR values saturate (SAR_{max}) around 3305 W/g_{Fe} (Table S1). In the H range of 5–20 kA/m, the SAR values of $Zn_{0.4}Fe_{2.6}O_4$@SiO_2-O clusters are similar to those reported for uncoated $Zn_{0.4}Fe_{2.6}O_4$ NPs (Figure 4a). Starting with H of 25 kA/m, the $Zn_{0.4}Fe_{2.6}O_4$@SiO_2-O clusters exhibit lower SAR values compared to uncoated counterparts, the SAR_{max} reaching 2600 W/g_{Fe} (Table S1). In the H range of

25–65 kA/m, the average difference between MH performances of uncoated and silica-coated $Zn_{0.4}Fe_{2.6}O_4$ clusters is 750 W/g_{Fe}. This big difference can be explained by the potential of uncoated $Zn_{0.4}Fe_{2.6}O_4$ NPs to organize in chains under the influence of the AMF. This type of organization increases the magnetic anisotropy of the assembly as compared to individual NPs, and it ultimately leads to an enhancement of the heating performances, as was previously reported for magnetite NPs with comparable sizes and magnetic properties [51]. On the contrary, the silica layer prevents the $Zn_{0.4}Fe_{2.6}O_4$ NPs within clusters from entering into physical contact and associating in long chains along the AMF lines. Alternatively, the silica coating increases the hydrodynamic diameters of clusters, reducing their Brownian motion and consequently, the SAR diminishes. However, a closer look at the TEM images in Figure 3a,b reveals that the $Zn_{0.4}Fe_{2.6}O_4$@SiO_2-O clusters are not spherical but rather elongated. The individual $Zn_{0.4}Fe_{2.6}O_4$ NPs inside these silica-coated clusters seem to be assembled in small chains (resembling magnetosomes) [52], a configuration that facilitates a good MH performance of $Zn_{0.4}Fe_{2.6}O_4$@SiO_2-O clusters. The SAR values reported for $Zn_{0.4}Fe_{2.6}O_4$@SiO_2-O clusters are superior as compared to individual $Zn_{0.4}Fe_{2.6}O_4$@SiO_2 NPs (15.39 kA/m, 525 kHz) [28] or $Zn_{0.5}Fe_{2.5}O_4$@SiO_2 NPs (5–30 kA/m, 430 kHz) [20]. On the other hand, for H of 15 kA/m (380 kHz), less coercive $Zn_{0.3}Fe_{2.7}O_4$ ferrites, individually coated in the SiO_2 layer, exhibit double SAR value (1010 W/g_{Fe}) [23]. Nevertheless, by increasing the H, the difference between SAR values is reduced, while for H of 35 kA/m the SAR values are almost identical [23].

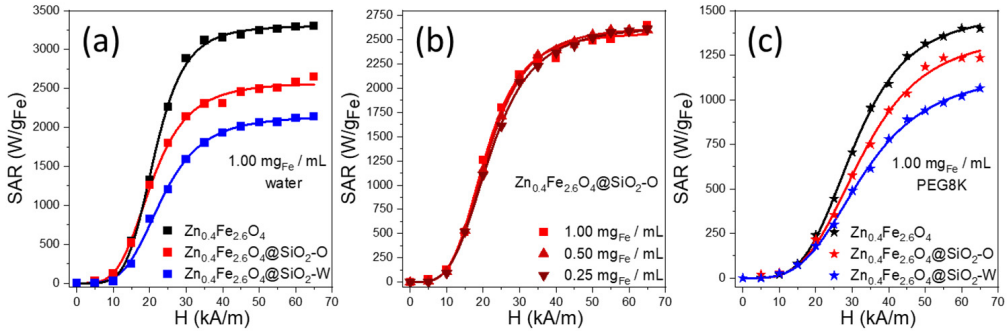

Figure 4. Field dependence of Specific Absorption Rate (SAR) for (**a**) $Zn_{0.4}Fe_{2.6}O_4$, $Zn_{0.4}Fe_{2.6}O_4$@SiO_2-W, and $Zn_{0.4}Fe_{2.6}O_4$@SiO_2-O clusters dispersed in water at 1.00 mg_{Fe}/mL; (**b**) $Zn_{0.4}Fe_{2.6}O_4$@SiO_2-O clusters dispersed in water at 1.00, 0.50, and 0.25 mg_{Fe}/mL; (**c**) $Zn_{0.4}Fe_{2.6}O_4$, $Zn_{0.4}Fe_{2.6}O_4$@SiO_2-W, and $Zn_{0.4}Fe_{2.6}O_4$@SiO_2-O clusters dispersed in PEG8K at 1.00 mg_{Fe}/mL. Curves represent the fits with the logistic function (Section S2).

Over the entire H range, the $Zn_{0.4}Fe_{2.6}O_4$@SiO_2-W clusters exhibit lower SAR values with respect to $Zn_{0.4}Fe_{2.6}O_4$@SiO_2-O clusters. The hyperthermia coercive field (H_{cHyp}) increased to 20.6 kA/m, while the SAR_{MAX} decreased by 500 W/g_{Fe} as compared to $Zn_{0.4}Fe_{2.6}O_4$@SiO_2-O clusters (Table S1). The distinctive hyperthermia performance of the two types of silica-coated clusters is related to the strength of magnetic dipole–dipole interaction manifested between $Zn_{0.4}Fe_{2.6}O_4$ NPs composing the clusters. Nanoencapsulation of a large number of $Zn_{0.4}Fe_{2.6}O_4$ NPs in a silica layer, as in the case of $Zn_{0.4}Fe_{2.6}O_4$@SiO_2-W clusters, leads to an increase of dipole–dipole interactions that is detrimental to SAR [10,53]. On the other hand, the small $Zn_{0.4}Fe_{2.6}O_4$@SiO_2-O clusters, have larger mobility and better colloidal stability under AMF. On the contrary, the big $Zn_{0.4}Fe_{2.6}O_4$@SiO_2-W clusters are prone to aggregation under the action of AMF as well as to sedimentation at the bottom of the vial, reducing the Brownian movement and hence the heating performance.

Weakly coercive F-MNPs usually exhibit an increase of SAR by decreasing the concentration, as dipole-dipole interactions are minimized [54–56]. The situation is the opposite for highly coercive F-MNPs for which the SAR values decrease with decreasing the concentration [57–59]. As can be seen in Figure 4b, there is no variation in SAR values with the concentration for $Zn_{0.4}Fe_{2.6}O_4$@SiO_2-O clusters. The saturation value of SAR (SAR_{Max}) and the hyperthermia coercive field (H_{cHyp}) remain almost constant when decreasing the

concentration from 1 mg_{Fe}/mL down to 0.25 mg_{Fe}/mL (Table S1). This is not the case for both $Zn_{0.4}Fe_{2.6}O_4$ and $Zn_{0.4}Fe_{2.6}O_4$@SiO_2-W clusters, where a variation of SAR values with the colloidal concentration has been recorded (data not shown). This experimental evidence suggests that the thick silica layer around Zn0.4Fe2.6O4 clusters inhibits the inherent magnetic dipole–dipole interactions [60] between them that are responsible for the SAR variation with the concentration, making the Zn0.4Fe2.6O4@SiO2-O clusters excellent candidates for in in vivo and in vitro experiments.

The suppression of magnetic dipole–dipole interactions between $Zn_{0.4}Fe_{2.6}O_4$@SiO_2-O clusters represents an advantage for in vitro MH experiments since this type of interaction in conjunction with reduced mobility of MNPs confined in endosomes inside the cytosol are responsible for their lower heating efficiency in vitro [61]. To obtain a realistic heating performance, the three types of clusters were immobilized in PEG8K. As plotted in Figure 4c, the SAR values of all three samples are reduced in comparison with water (Figure 4a). In general, the SAR reduction is 80–85% for H of 15 kA/m, and it diminishes to 50–55% by increasing H to 65 kA/m. On average, over the entire H range, a reduction of SAR by 68%, 65%, and 62% for $Zn_{0.4}Fe_{2.6}O_4$ NPs, $Zn_{0.4}Fe_{2.6}O_4$@SiO_2-O clusters, and $Zn_{0.4}Fe_{2.6}O_4$@SiO_2-W clusters, respectively, were recorded. These observations suggest that the Brownian relaxation mechanism is the main heating mechanism of both types of silica-coated clusters (in the liquid phase), as demonstrated for the mesoscale assemblage of iron oxide nanocubes [53]. Similar to the aqueous medium, the SAR values in PEG8K of both $Zn_{0.4}Fe_{2.6}O_4$ and $Zn_{0.4}Fe_{2.6}O_4$@SiO_2-O clusters are identical up to H of 20 kA/m. From 25 kA/m to 65 kA/m, a small average difference of 150 W/g_{Fe} is observed in favor of uncoated $Zn_{0.4}Fe_{2.6}O_4$ clusters. The immobilization of uncoated $Zn_{0.4}Fe_{2.6}O_4$ NPs in PEG restricts their association in chains, and hence reduces the difference between their MH performances and those of $Zn_{0.4}Fe_{2.6}O_4$@SiO_2-O clusters by a factor of five. Since chain formation is hindered by the silica layer, comparing the MH performances of two types of silica-coated clusters showed that the average difference of SAR values decreased only by a factor of three, from 480 W/g_{Fe} in water to 160 W/g_{Fe} in PEG8K. As observed from Figure 4c, the average value of SAR, in PEG 8 K and on H ranging from 25 to 65 kA/m, decreases progressively by 150–160 W/g_{Fe}, when passing from uncoated $Zn_{0.4}Fe_{2.6}O_4$ NPs to small $Zn_{0.4}Fe_{2.6}O_4$@SiO_2-O clusters and finally to big $Zn_{0.4}Fe_{2.6}O_4$@SiO_2-W clusters. Since the Brownian motion is suppressed in the solid matrix (PEG8K), the progressive reduction of SAR values can be mainly attributed to the increased strength of magnetic dipole–dipole interactions manifested between $Zn_{0.4}Fe_{2.6}O_4$ NPs within the three types of clusters. Since the $Zn_{0.4}Fe_{2.6}O_4$@SiO_2-O clusters exhibit the best MF performance among the two types of silica-coated clusters, they were further tested in vitro on a cancer cell line in conjunction with uncoated $Zn_{0.4}Fe_{2.6}O_4$ clusters.

3.4. Cellular Internalization and Cytotoxicity

The reaction of digestion-free ferric ions with thiocyanate was used to quantitatively evaluate the internalization of both $Zn_{0.4}Fe_{2.6}O_4$ NPs and $Zn_{0.4}Fe_{2.6}O_4$@SiO_2-O clusters on the A549 and BJ cells. The relative internalization as a function of dosage level (Figure 5a) showed that almost all $Zn_{0.4}Fe_{2.6}O_4$@SiO_2-O clusters were internalized for the first three doses (15, 31, and 62.5 μg/cm^2). As indicated in Figure 5b, the iron amount increased twice (60 to 128 μg/well) and then four times (60 to 236 μg/well), as the exposure dose was increased from 15 μg/cm^2 to 31 μg/cm^2 and 62.5 μg/cm^2, respectively. This is translated into a linear dependence of the total iron amount internalized in cells with the dosage level (Figure 5c). By further increasing the exposure dose to 125 μg/cm^2, a considerable drop of 35% in the relative internalization was recorded (Figure 5a). At the highest tested dose (250 μg/cm^2), the relative internalization continued to decrease, going below 40%. The iron amount internalized in cells deviated from the linear dose dependence and saturated around 375 μg_{Fe}/well (310 pg_{Fe}/cell) (Figure 5c). Compared with silica-coated iron oxide clusters that we previously investigated [41], a higher relative internalization was achieved for the $Zn_{0.4}Fe_{2.6}O_4$@SiO_2-O clusters. Congruent results were

reported for SPIONs modified with non-porous and mesoporous silica [62]. The exposure of A549 cells to a dose equivalent to 6.25 μg/cm^2 resulted in a cellular Fe content ranging from 20–25 pg$_{Fe}$/cell [62], which would be similar to the present study (20 pg$_{Fe}$/cell at a dose of 62.5 μg/cm^2 taking into account a relative internalization > 95%). In comparison with single-core containing $Zn_xFe_{3-x}O_4$@SiO_2 NPs, where an Fe content of approximately 60 pg$_{Fe}$/cell was observed after a 12 h incubation with an equivalent dose of 600 μg/cm^2, the $Zn_{0.4}Fe_{2.6}O_4$@SiO_2-O clusters exhibited a much higher cellular internalization [20]. Compared with silica-coated iron oxide clusters that we previously investigated [41], a slightly higher relative internalization was achieved for the $Zn_{0.4}Fe_{2.6}O_4$@SiO_2-O clusters for doses from 15 to 62.5 μg/cm^2. Independently of the dose used, the BJ cells display a statistically lower cellular internalization (Figure 5a,b). While for the first three doses (15, 31, and 62.5 μg/cm^2) the relative internalization of $Zn_{0.4}Fe_{2.6}O_4$@SiO_2-O clusters in A549 cells is close to 100%, the relative internalization started at 86% and slightly decreased to 64% in the case of BJ cells. A high drop in the relative internalization (38%) is recorded for a dosage level of 125 μg/cm^2, while continuing to diminish to 23% for the highest dose (250 μg/cm^2). No saturation effect has been observed for BJ cells, the internalized iron amount per well followed a progressively increased from 60 to 255 μg/well by increasing the dose (Figure 5b). Due to a higher cytoplasmatic volume of BJ cells, the cell plate accommodates lower cells number as compared to A549 cells. In this condition, the internalized amount per BJ cell was approximately double (Figure 5c).

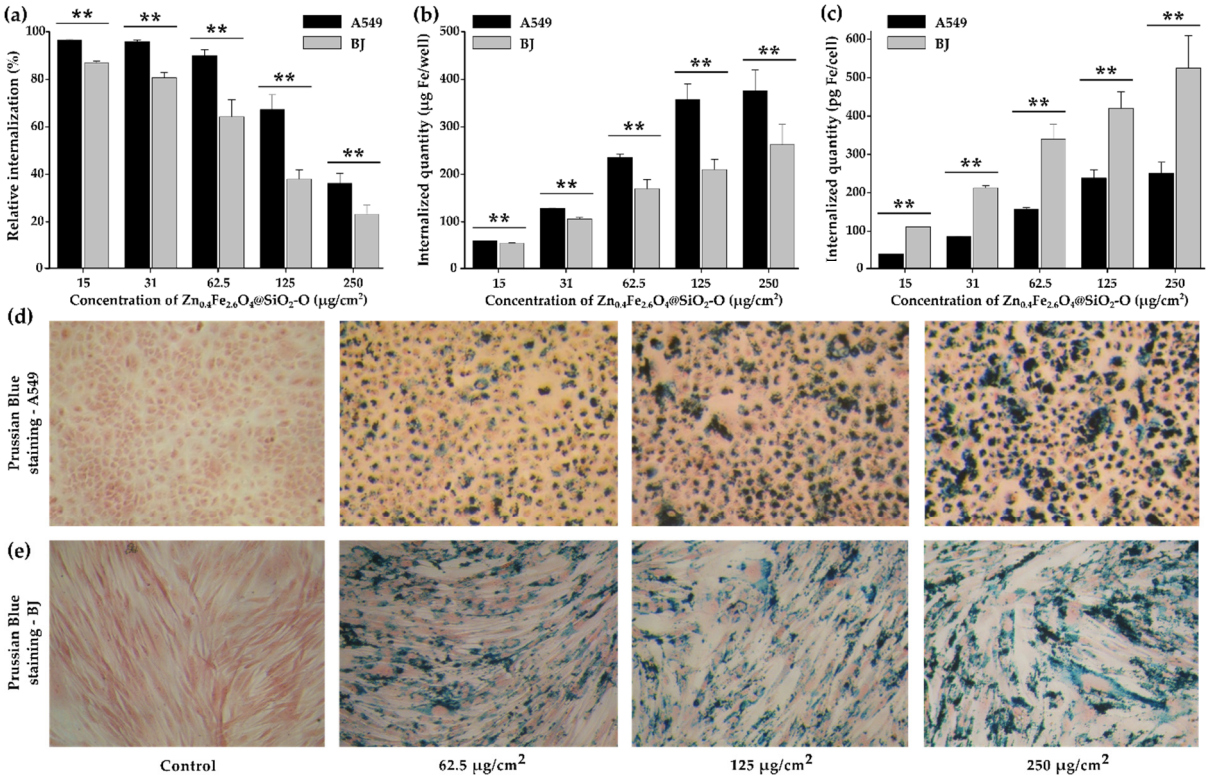

Figure 5. Cellular internalization of $Zn_{0.4}Fe_{2.6}O_4$@SiO_2-O clusters in A549 and BJ cells after a 24 h exposure: (**a**) the relative internalization and (**b**) total iron amount per well and per cell. (**c**) total iron amount per cell. Prussian Blue staining of (**d**) A549 and (**e**) cells exposed for 24 h to $Zn_{0.4}Fe_{2.6}O_4$@SiO_2-O clusters. Values are expressed as mean ± SD of three biological replicates. Double asterisks (**) indicate a significant difference with p values < 0.001 (ANOVA + Dunn's).

The relative internalization for uncoated $Zn_{0.4}Fe_{2.6}O_4$ clusters is only 59% for the smallest dose of 15 μg/cm^2, and it decreases to 11% for the highest dose of 125 μg/cm^2 (Figure S5). For the BJ cells, the relative internalization is even lower, decreasing from 25% to 5% over the dose range (Figure S5a). In terms of the internalized iron amount per

well, a constant value at approximately 21 μg/well for the first three doses and increasing up to 73 μg/well for the highest dose (Figure S5b) is observed for BJ cells. In the case of A549 cells, the iron amount internalized per well is much higher, ranging from 50 to 123 μg/well over the dose range (Figure S5b). However, when counting the internalized iron amount per cell, there is no difference between the two cell lines for the first three doses (Figure S5c). From a dosage level of 125 μg/cm^2, the BJ cells accommodate more uncoated $Zn_{0.4}Fe_{2.6}O_4$ clusters than the A549 cells (Figure S5c). All these observations clearly point out that the coating with silica increased the cellular internalization of the $Zn_{0.4}Fe_{2.6}O_4$ NPs by a factor of 1.7 to 3, as the dosage level is increased from 15 to 125 μg/cm^2. Following nanostructures adsorption on the cellular membrane, internalization occurs through a variety of processes, including pinocytosis, non-specific or receptor-mediated endocytosis, and phagocytosis [63], while the dimension of the nanostructure represents a key factor in cellular internalization. In addition, the $Zn_{0.4}Fe_{2.6}O_4$@SiO_2-O clusters exhibit a less negative zeta potential (−27 mV) than uncoated $Zn_{0.4}Fe_{2.6}O_4$ clusters (−52 mV). The lower zeta potential could facilitate the adsorption of the $Zn_{0.4}Fe_{2.6}O_4$@SiO_2-O clusters to the A549 cell membranes as they display extensive negative charged domains that electrostatically repel highly negatively charged NPs [64–66].

The $Zn_{0.4}Fe_{2.6}O_4$@SiO_2-O clusters were indeed effectively internalized by A549 and BJ cells, as revealed by the light microscopic images where agglomerates of $Zn_{0.4}Fe_{2.6}O_4$@SiO_2-O clusters are visible in the cytoplasm (Figure 5d,e). Regardless of the dosage level of $Zn_{0.4}Fe_{2.6}O_4$@SiO_2-O clusters, the A549 cells exhibited typical morphology with no shrinkage of the cellular volume, indicative of a cytotoxic effect (Figure 5d,e). A dose-dependent internalization process can be observed by a closer inspection of images. Moreover, a perinuclear deposition of the nanomaterials was observed for both types of cells, with almost no particles being observed in the nuclear area. At the same time, it can be observed that the cytoplasmatic loading with $Zn_{0.4}Fe_{2.6}O_4$@SiO_2-O clusters was not uniformly realized. A similar observation can be drawn for uncoated $Zn_{0.4}Fe_{2.6}O_4$ when inspecting their corresponding images presented in Figure S5d,e. In addition, the poor internalization of uncoated $Zn_{0.4}Fe_{2.6}O_4$ NPs with respect to $Zn_{0.4}Fe_{2.6}O_4$@SiO_2-O clusters can be also identified at each dosage level.

The viability of A549 cancer and BJ normal cells was determined by Alamar Blue (AB) and Neutral Red (NR) assays after incubation for 24 h with various concentrations of $Zn_{0.4}Fe_{2.6}O_4$@SiO_2-O clusters (Figure 6a,b) and of uncoated $Zn_{0.4}Fe_{2.6}O_4$ clusters (Figure S6a,b) ranging from 15 to 250 μg/cm^2 (50–800 μg/mL). Cells that were not exposed to $Zn_{0.4}Fe_{2.6}O_4$@SiO_2-O clusters were used as a negative control. Similar to our previously published studies, the optical and the biochemical interferences were firstly evaluated to avoid artefactual data caused by the interferences of $Zn_{0.4}Fe_{2.6}O_4$@SiO_2-O clusters with the biochemical assays used [41,59,67]. At a dosage level of 15 μg/cm^2, the AB assay did not exhibit statistically relevant cytotoxicity (Figure 6a). A slight statistical decrease in viability is recorded by increasing the dosage level (Figure 6a). Even though for doses from 31 to 125 μg/cm^2 the viability of cells is slightly lower than that of the control group, it is still well above 80%, which is considered the viability threshold for nanomaterials to be safe for biomedical applications [68]. For 250 μg/cm^2, the $Zn_{0.4}Fe_{2.6}O_4$@SiO_2 clusters exhibited relevant cytotoxicity, decreasing cellular viability by more than 20% (Figure 6a). Instead, at this dosage level, the viability of BJ cells was still slightly above 80% (Figure 6b). Taking into account that the BJ cells accommodate a double number of silica-coated clusters, the toxicity level of these nanostructures toward normal cells is much lower compared to A549 cells. Conversely, the NR assay displayed an increase in cellular viability starting with the lowest dose (Figure 6a,b). The highest increase in cellular viability was observed at intermediary doses, which did not induce a cytotoxic effect based on the AB assay (Figure 6a,b). At the highest tested dose of 250 μg/cm^2, the viability was not different from that observed for the negative control for both cell lines. As observed by our group and others, these slight increases in viability measured with the NR assay are most probably due to the increase in the lysosomal compartment that favors the ATP-dependent incorporation of

the NR dye in the cells [69,70]. Similarly, an increase in cellular viability based on the NR data and a decrease in viability according to the WST assay was reported by another group for magnetite NPs [70]. The $Zn_{0.4}Fe_{2.6}O_4$@SiO_2-O clusters are less toxic, compared to silica-coated iron oxide clusters of bigger dimensions (threshold dose of 125 μg/cm^2) [41], and they exhibit higher toxicity with respect to the single-core containing $Zn_xFe_{3-x}O_4$@SiO_2 NPs, which showed biocompatibility up to 1000 μg/mL [16,20,23]. Due to the pure internalization of uncoated $Zn_xFe_{3-x}O_4$ clusters in both types of cells, according to the AB assay, no cytotoxicity effect was recorded over the entire dose interval (Figure S6a,b). Similar to the case of $Zn_{0.4}Fe_{2.6}O_4$@SiO_2-O clusters, the NR assay indicated an increase in cellular viability mainly at intermediate doses (Figure S6a,b).

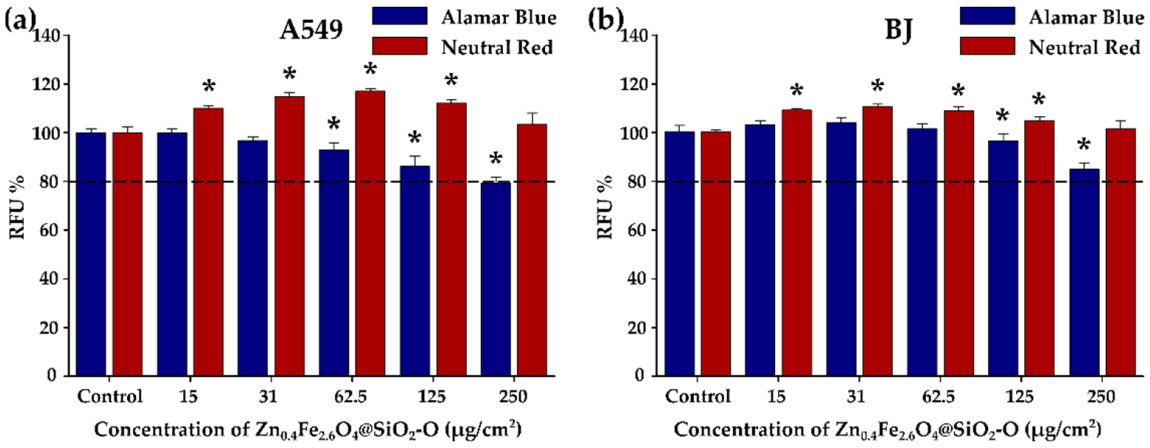

Figure 6. Cytocompatibility of $Zn_{0.4}Fe_{2.6}O_4$@SiO_2-O clusters on (**a**) A549 and (**b**) BJ cell line after a 24 h exposure. Data are presented as relative fluorescence units (RFU) as compared to the negative control (100%), as mean ± SD of three biological replicates. The significant differences compared to the negative control (ANOVA + Dunn's; $p < 0.05$) are noted with asterisks (*).

3.5. In Vitro Magnetic Hyperthermia

A549 and BJ cells were incubated with $Zn_{0.4}Fe_{2.6}O_4$@SiO_2-O clusters in a concentration range from 31 to 125 μg/cm^2 for 24 h and then exposed for 30 min to an AMF of variable amplitude (15, 20, and 30 kA/m) and a fixed frequency of 355 kHz. The effect of AMF was evaluated by measuring cellular viability with respect to a control sample by performing both AB and NR assays 24 h after MH treatments. The effect of AMF alone was also evaluated by exposing untreated A549 cells, following the same protocol applied to A549 cells containing $Zn_{0.4}Fe_{2.6}O_4$@SiO_2-O clusters. This latter exposure was accompanied by a modest increase in temperature, not exceeding 0.5 °C, which did not affect cellular viability [41,59]. The heating curves of A549 cells containing internalized $Zn_{0.4}Fe_{2.6}O_4$@SiO_2-O clusters exhibited a relevant increase in the temperature in the first 5 min followed by the formation of a plateau (Figure S7). The saturation temperature (T_s) strongly depends on the amount of internalized $Zn_{0.4}Fe_{2.6}O_4$@SiO_2-O clusters as well as on the amplitude of AMF (Figure S7), and it can be correlated with cellular viability (Figure 7). Both toxicity assays indicated no changes in cellular viability for a dosage level of 31 and 62.5 μg/cm^2 at H of 15 kA/m (Figure 7a). This is congruent to small T_s values of 39.7 and 41.1 °C reached during MH treatment (Figure S7), which are below the 42 °C considered to be the threshold value necessary to initialize apoptosis in cancer cells. For a dose of 125 μg/cm^2, the T_s increased up to 42.7 °C. At this point, the NR assay indicated a minor change in cellular viability, while the AB assay showed that approximately a quarter of the A549 cells were dead (Figure 7a). For normal cells, no cytotoxic effect was observed for all three doses at an H of 15 kA/m (Figure 7b), the recorded T_s being well below 42 °C (Figure S7). The effect of MH treatment in killing A549 cells became relevant at H of 20 kA/m, above the coercive field of $Zn_{0.4}Fe_{2.6}O_4$ NPs (15 kA/m). Firstly, for a dose of 31 μg/cm^2, cellular viability decreased to 67% according to the AB assay, while the NR assay

indicated only a 10% drop in cellular viability. The low percentage of damaged cells can be explained by the T_s of 43 °C, which is not enough to induce a statistically major decrease in cellular viability upon 24 h from MH treatment. For the next two doses of 62.5 μg/cm^2 and 125 μg/cm^2, the AMF exposure at 20 kA/m enabled reaching T_s of 45.3 °C and 47.5 °C, respectively. Consequently, the MH treatment-induced cellular death in more than 90% of A549 cells, as independently indicated by both biochemical assays. A cytotoxic effect was also recorded for BJ cells exposed at H of 20 kA/m; however, the percentages of dead cells were smaller (Figure 7b) compared to A549 cells. For the first dose (31 μg/cm^2), the T_s reached a value of 42 °C, which was not enough to produce a cytotoxic effect (Figure 7b). Starting from the intermediary dose of 62.5 μg/cm^2, AB and NR assays exhibited a 35% and a 15% decrease in viability, respectively (Figure 7b), which indicates a minor cytotoxic effect in accordance with the reached T_s of 43.5 °C (Figure S7). The cytotoxic effect was relevant at the highest exposure dose (125 μg/cm^2), the viability decreasing to 20% and 50% based on the AB and NR data, respectively (Figure 7b). Independent of the cell type and the viability assay used, the MH treatment at H of 30 kA/m enabled reaching T_s well above 45 °C (Figure S7). As a consequence, the viabilities indicated a cellular death of more than 90% of cells (Figure 7a,b).

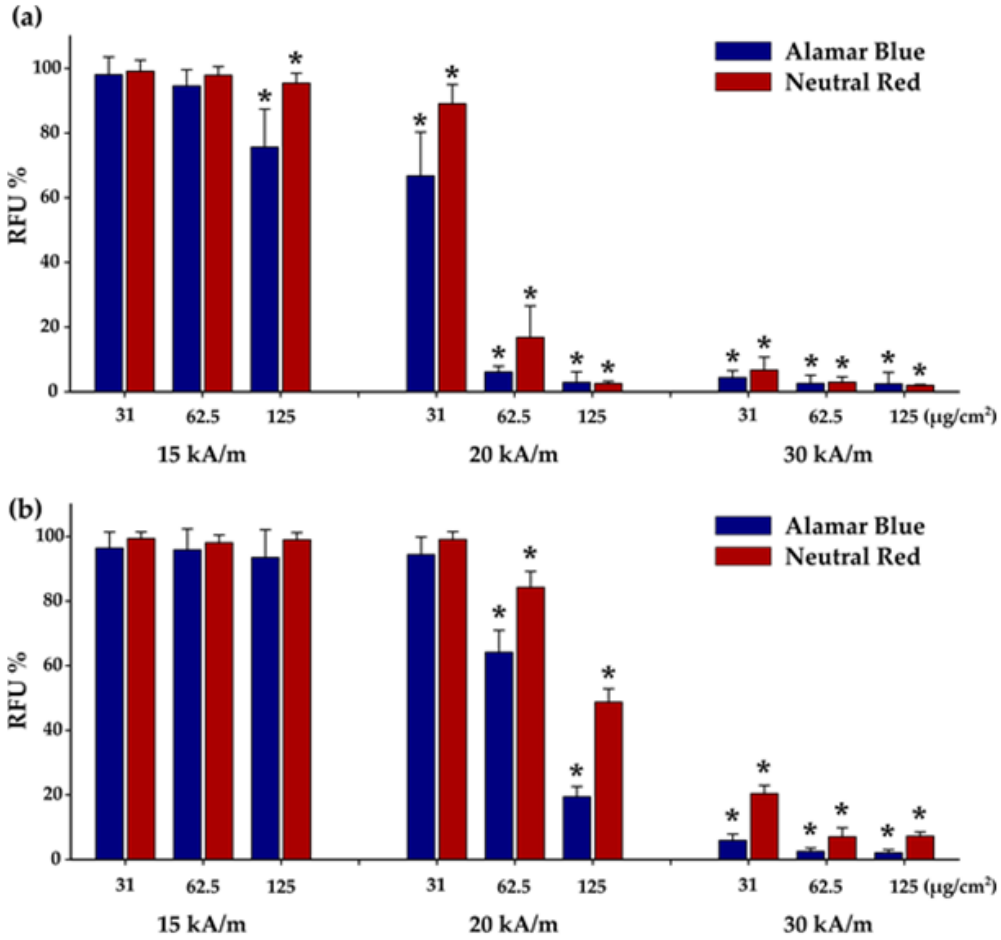

Figure 7. Cytotoxic effects of internalized $Zn_{0.4}Fe_{2.6}O_4$@SiO_2-O clusters in (**a**) A549 and (**b**) BJ cells were evaluated after a 30 min exposure to AMF of 355 kHz and amplitudes of 15, 20, and 30 kA/m. Cellular viability was measured using Alamar Blue and Neutral Red assays and presented as the mean ± SD of three biological replicates. Data are presented as relative values to AMF negative control (100%). The significant differences compared to the negative control (ANOVA + Dunn's; $p < 0.05$) are marked with asterisks (*).

The cellular viability data obtained using both biochemical assays followed a sigmoidal dependence as a function of T_s (Figure S8a), which can be fitted by an equation derived from a two-state model of temperature-dependent cell damage [71]. The fitting results indicated that the temperatures at which the A549 cells, exposed for 30 min to MH treatment, received a 50% lethal dose (LD50%) are 43.44 °C and 44.69 °C for the AB and the NR assays, respectively (Figure S8a). These values are very close to those obtained in previous studies [41,67]. A second important parameter resulting from the fits is the temperature width for a given decrease in cell viability. Both biochemical assays revealed a temperature width of 0.75 °C (Figure S8a), which means that the distribution of A549 cells with different responses to MH treatment is narrow. In other words, the 100% decrease in cellular viability occurs in a temperature interval of less than 1 °C, once initiated through the heat generated by the internalized $Zn_{0.4}Fe_{2.6}O_4$@SiO_2-O clusters. In the case of BJ cells, the AB and the NR assays showed that a 50% lethal dose was reached at a temperature of 44.22 °C and 45.46 °C, respectively, while a complete destruction (100%) can occur in a temperature interval of 1 °C. Consequently, the BJ cells are more resilient to MH treatment as compared to A549 cells using $Zn_{0.4}Fe_{2.6}O_4$@SiO_2-O clusters as nanoheaters.

4. Conclusions

We have developed a new straightforward method for silica coating of pre-existing clusters of ferromagnetic nanoparticles (F-MNPs) formed by cubic Zn ferrite nanoparticles (NPs). Compared to classical methods of silica coating based on the Stöber process or water-in-oil microemulsion, our method is fast, facile, effective, and eco-friendly. The silica (SiO_2) coating method resides in using an oil-in-water microemulsion and ultrasounds, which allowed us to obtain $Zn_{0.4}Fe_{2.6}O_4$@SiO_2 clusters in 30 min, displaying a small hydrodynamic diameter of 145 nm. The produced $Zn_{0.4}Fe_{2.6}O_4$@SiO_2-O clusters exhibit high heating power when exposed to an alternating magnetic field (AMF) of 355 kHz and variable amplitudes. The Specific Absorption Rate (SAR) increased sigmoidally, with the AMF amplitude reaching a saturation value of 2600 W/g_{Fe}. The SAR values did not vary with the colloidal concentration (in the range of 0.25–1 mg/mL), proving that the silica coating significantly reduces the magnetostatic interactions among coercive $Zn_{0.4}Fe_{2.6}O_4$ clusters.

Cytotoxicity studies on the A549 cancer cell line using two complementary assays (Alamar Blue and Neutral Red) revealed a good biocompatibility with a drop of only 22% in cellular viability at the highest dose of 250 $\mu g/cm^2$ (0.8 mg/mL) used. Instead, insignificant toxicity for normal BJ cells was recorded. Cellular uptake experiments revealed that $Zn_{0.4}Fe_{2.6}O_4$@SiO_2-O clusters are internalized in A549 cells in a linear dose-dependent manner and then saturated at higher doses. BJ cells internalized double the amount of $Zn_{0.4}Fe_{2.6}O_4$@SiO_2-O clusters per cell, however the relative internalization indicated a smaller cellular uptake as compared to A549 cells. Moreover, the cellular uptake is almost three times higher as compared to the uncoated NPs. This higher uptake is translated into a high intracellular magnetic hyperthermia efficiency, our results revealing that more than 90% of A549 cells, incubated at a dose of 62.5 $\mu g/cm^2$, underwent cellular death close to the upper limits of safe AMF field conditions (20 kA/m, 355 kHz). The sigmoidal fitting of cellular viability as a function of saturation temperature revealed that the LD50% in A549 cells was at a mean temperature of 44 °C. The BJ cells were found to be more resilient to MH treatment, the threshold dose being 125 $\mu g/cm^2$ at the same AMF condition (20 kA/m, 355 kHz), while LD50% was initiated at a mean temperature of 45 °C.

The silica coating methodology elaborated herein is not limited to the use of coercive $Zn_{0.4}Fe_{2.6}O_4$ NPs as core constituents, therefore extensions to other types of NPs may yield new hybrid nano-objects. The suppression of strong magnetostatic interactions by the silica layer and the fact that the silica-coated clusters are easy to disperse in water, open up the coercive MNPs for a large range of applications. Moreover, the silica surface of the clusters offers multiple possibilities for further functionalization, either by targeting ligands or by chemotherapeutic drugs opening multiple ways for biomedical applications.

The high heating performances of the developed $Zn_{0.4}Fe_{2.6}O_4$ NPs in conjunction with the scalability of the oil-in-water microemulsion silica coating procedure could facilitate a successful implementation of the $Zn_{0.4}Fe_{2.6}O_4$@SiO_2-O clusters into clinical applications.

Supplementary Materials: The following supporting information can be downloaded at: https://www.mdpi.com/article/10.3390/biomedicines10071647/s1, Figures S1–S3: Heating curves and their corresponding temperature change ΔT versus time curves fitted with Box–Lucas equation; Figure S4: Calibration curve for iron concentration determination; Figure S5: Cellular internalization of uncoated $Zn_{0.4}Fe_{2.6}O_4$ clusters; Figure S6: Cytotoxicity of uncoated $Zn_{0.4}Fe_{2.6}O_4$ clusters; Figure S7: Heating curves of in vivo MH treatment; Figure S8: Cellular viability versus saturation temperature; Table S1: Fitting parameters of SAR evolution with H.

Author Contributions: Conceptualization, S.N. and C.I.; methodology, S.N., I.F. and C.I.; software, S.N. and C.I.; validation S.N., I.F., F.L., N.V., C.M.L. and C.I.; formal analysis, S.N., I.F., R.D., L.B.-T., A.P., C.M.L. and C.I.; investigation, S.N., I.F., R.D., L.B.-T., A.P. and C.I.; resources, C.I.; data curation, S.N., I.F., N.V., C.M.L. and C.I.; writing—original draft preparation, S.N., I.F., C.M.L. and C.I.; writing—review and editing, S.N., I.F., C.M.L. and C.I.; visualization, S.N., I.F., C.M.L. and C.I.; supervision, F.L., C.M.L. and C.I.; project administration, C.I.; funding acquisition, C.I. All authors have read and agreed to the published version of the manuscript.

Funding: This research was funded by two grants from the Romanian Ministry of Education and Research, CNCS—UEFISCDI, project numbers PN-III-P2-2.1-PED-2019-3283 and PN-III-P1-1.1-TE-2019-1392, within PNCDI III.

Institutional Review Board Statement: Not applicable.

Informed Consent Statement: Not applicable.

Data Availability Statement: Not applicable.

Conflicts of Interest: The authors declare no conflict of interest. The funders had no role in the design of the study; in the collection, analyses, or interpretation of data; in the writing of the manuscript, or in the decision to publish the results.

References

1. Wlodarczyk, A.; Gorgon, S.; Radon, A.; Bajdak-Rusinek, K. Magnetite Nanoparticles in Magnetic Hyperthermia and Cancer Therapies: Challenges and Perspectives. *Nanomaterials* **2022**, *12*, 1807. [CrossRef]
2. Mokhosi, S.R.; Mdlalose, W.; Nhlapo, A.; Singh, M. Advances in the Synthesis and Application of Magnetic Ferrite Nanoparticles for Cancer Therapy. *Pharmaceutics* **2022**, *14*, 937. [CrossRef]
3. Kulikov, O.A.; Zharkov, M.N.; Ageev, V.P.; Yakobson, D.E.; Shlyapkina, V.I.; Zaborovskiy, A.V.; Inchina, V.I.; Balykova, L.A.; Tishin, A.M.; Sukhorukov, G.B.; et al. Magnetic Hyperthermia Nanoarchitectonics via Iron Oxide Nanoparticles Stabilised by Oleic Acid: Anti-Tumour Efficiency and Safety Evaluation in Animals with Transplanted Carcinoma. *Int. J. Mol. Sci.* **2022**, *23*, 4234. [CrossRef]
4. Nguyen, L.H.; Phong, P.T.; Nam, P.H.; Manh, D.H.; Thanh, N.T.K.; Tung, L.D.; Phuc, N.X. The Role of Anisotropy in Distinguishing Domination of Néel or Brownian Relaxation Contribution to Magnetic Inductive Heating: Orientations for Biomedical Applications. *Materials* **2021**, *14*, 1875. [CrossRef]
5. Ota, S.; Kitaguchi, R.; Takeda, R.; Yamada, T.; Takemura, Y. Rotation of Magnetization Derived from Brownian Relaxation in Magnetic Fluids of Different Viscosity Evaluated by Dynamic Hysteresis Measurements over a Wide Frequency Range. *Nanomaterials* **2016**, *6*, 170. [CrossRef]
6. Morales, I.; Costo, R.; Mille, N.; Da Silva, G.B.; Carrey, J.; Hernando, A.; De la Presa, P. High Frequency Hysteresis Losses on γ-Fe_2O_3 and Fe_3O_4: Susceptibility as a Magnetic Stamp for Chain Formation. *Nanomaterials* **2018**, *8*, 970. [CrossRef]
7. Tong, S.; Quinto, C.A.; Zhang, L.; Mohindra, P.; Bao, G. Size-Dependent Heating of Magnetic Iron Oxide Nanoparticles. *ACS Nano* **2017**, *11*, 6808–6816. [CrossRef]
8. Hugounenq, P.; Levy, M.; Alloyeau, D.; Lartigue, L.; Dubois, E.; Cabuil, V.; Ricolleau, C.; Roux, S.; Wilhelm, C.; Gazeau, F.; et al. Iron oxide monocrystalline nanoflowers for highly efficient magnetic hyperthermia. *J. Phys. Chem. C* **2012**, *116*, 15702–15712. [CrossRef]
9. Mohapatra, J.; Zeng, F.; Elkins, K.; Xing, M.; Ghimire, M.; Yoon, S.; Mishrab, S.R.; Ping Liu, J. Size-dependent magnetic and inductive heating properties of Fe3O4 nanoparticles: Scaling laws across the superparamagnetic size. *Phy. Chem. Chem. Phys.* **2018**, *20*, 12879–12887. [CrossRef]

10. Coral, D.F.; Mendoza Zélis, P.; Marciello, M.; del Puerto Morales, M.; Craievich, A.; Sanchez, F.H.; Fernandez van Raap, M.B. Effect of nanoclustering and dipolar interactions in heat generation for magnetic hyperthermia. *Langmuir* **2016**, *32*, 1201–1213. [CrossRef]
11. Serantes, D.; Baldomir, D.; Martinez-Boubeta, C.; Simeonidis, K.; Angelakeris, M.; Natividad, E.; Castro, M.; Mediano, A.; Chen, D.-X.; Sanchez, A.; et al. Influence of dipolar interactions on hyperthermia properties of ferromagnetic particles. *J. Appl. Phys.* **2010**, *108*, 073918. [CrossRef]
12. Tapeinos, C.; Tomatis, F.; Battaglini, M.; Larranaga, A.; Marino, A.; Agirrezabal-Telleria, I.; Angelakeris, M.; Debellis, D.; Drago, F.; Brero, F.; et al. Cell Membrane-Coated Magnetic Nanocubes with a Homotypic Targeting Ability Increase Intracellular Temperature due to ROS Scavenging and Act as a Versatile Theranostic System for Glioblastoma Multiforme. *Adv. Health Mater.* **2019**, *8*, e1900612. [CrossRef]
13. Castellanos-Rubio, I.; Rodrigo, I.; Olazagoitia-Garmendia, A.; Arriortua, O.; Gil de Muro, I.; Garitaonandia, J.S.; Bilbao, J.R.; Fdez-Gubieda, M.L.; Plazaola, F.; Orue, I.; et al. Highly Reproducible Hyperthermia Response in Water, Agar, and Cellular Environment by Discretely PEGylated Magnetite Nanoparticles. *ACS Appl. Mater. Interfaces* **2020**, *12*, 27917–27929. [CrossRef]
14. Guerro-Martinez, A.; Perez-Juste, J.; Liz-Marzan, L.M. Recent Progress on Silica Coating of Nanoparticles and Related Nanomaterials. *Adv. Mater.* **2010**, *22*, 1182–1195. [CrossRef]
15. Iliasov, A.R.; Nizamov, T.R.; Naumenko, V.A.; Garanina, A.S.; Vodopyanov, S.S.; Nikitin, A.A.; Pershina, A.G.; Chernysheva, A.A.; Kan, Y.; Mogilnikov, P.S.; et al. Non-magnetic shell coating of magnetic nanoparticles as key factor of toxicity for cancer cells in a low frequency alternating magnetic field. *Colloids Surf. B Biointerfaces* **2021**, *206*, 111931. [CrossRef]
16. Gao, Z.; Ring, L.H.; Sharma, A.; Namsrai, B.; Tran, N.; Finger, E.B.; Garwood, M.; Haynes, C.L.; Bischof, J.C. Preparation of Scalable Silica-Coated Iron Oxide Nanoparticles for Nanowarming. *Adv. Sci.* **2020**, *7*, 1901624. [CrossRef]
17. Rho, W.-Y.; Kim, H.-M.; Kyeong, S.; Kang, Y.-L.; Kim, D.-H.; Kang, H.; Jeong, C.; Kim, D.; Lee, E.; Jun, S.B.-H. Facile synthesis of monodispersed silica-coated magnetic nanoparticles. *J. Ind. Eng. Chem.* **2014**, *20*, 2646–2649. [CrossRef]
18. Marcelo, G.; Perez, E.; Corrales, T.; Peinado, C. Stabilization in Water of Large Hydrophobic Uniform Magnetite Cubes by Silica Coating. *J. Phys. Chem. C* **2011**, *115*, 25247–25256. [CrossRef]
19. Dai, Q.; Lam, M.; Swanson, S.; Rachel Yu, R.-H.; Milliron, D.J.; Topuria, T.; Jubert, P.-O.; Nelson, A. Monodisperse Cobalt Ferrite Nanomagnets with Uniform Silica Coatings. *Langmuir* **2010**, *26*, 17546–17551. [CrossRef]
20. Wang, R.; Liu, J.; Liu, Y.; Zhong, R.; Yu, X.; Liu, Q.; Zhang, L.; Lv, C.; Mao, K.; Tang, P. The cell uptake properties and hyperthermia performance of Zn0.5Fe2.5O4/SiO2 nanoparticles as magnetic hyperthermia agents. *R. Soc. Open Sci.* **2020**, *7*, 191139. [CrossRef]
21. Mathieu, P.; Coppel, Y.; Respaud, M.; Nguyen, Q.T.; Boutry, S.; Laurent, S.; Stanicki, D.; Henoumont, C.; Novio, F.; Lorenzo, J.; et al. Silica Coated Iron/Iron Oxide Nanoparticles as a Nano-Platform for T2 Weighted Magnetic Resonance Imaging. *Molecule* **2019**, *24*, 4629. [CrossRef] [PubMed]
22. Kolosnjaj-Tabi, J.; Kralj, S.; Griseti, E.; Nemec, S.; Wilhelm, C.; Sangnier, A.P.; Bellard, E.; Fourquaux, I.; Golzio, M.; Rols, M.-P. Magnetic Silica-Coated Iron Oxide Nanochains as Photothermal Agents, Disrupting the Extracellular Matrix, and Eradicating Cancer Cells. *Cancers* **2019**, *11*, 2040. [CrossRef]
23. He, S.; Zhang, H.; Liu, Y.; Sun, F.; Yu, X.; Li, X.; Zhang, L.; Wang, L.; Mao, K.; Wang, G.; et al. Maximizing Specific Loss Power for Magnetic Hyperthermia by Hard–Soft Mixed Ferrites. *Small* **2018**, *14*, 1800135. [CrossRef] [PubMed]
24. Singh, R.K.; Kim, T.-H.; Patel, K.D.; Knowles, J.C.; Kim, H.-W. Biocompatible magnetite nanoparticles with varying silica-coating layer for use in biomedicine: Physicochemical and magnetic properties, and cellular compatibility. *J. Biomed. Mater. Res. A* **2012**, *100A*, 1734–1742. [CrossRef]
25. Glaria, A.; Soule, S.; Hallali, N.; Ojo, W.; Mirjolet, S.M.; Fuks, G.; Cornejo, A.; Allouche, J.; Dupin, J.C.; Martinez, H.; et al. Silica coated iron nanoparticles: Synthesis, interface control, magnetic and hyperthermia properties. *RSC Adv.* **2018**, *8*, 32146–32156. [CrossRef]
26. Cannas, C.; Musinu, A.; Ardu, A.; Orru, F.; Peddis, D.; Casu, M.; Sanna, R.; Angius, F.; Diaz, G.; Piccaluga, G. $CoFe_2O_4$ and $CoFe_2O_4/SiO_2$ Core/Shell Nanoparticle: Magnetic and Spectroscopic Study. *Chem. Mater.* **2010**, *22*, 3353–3361. [CrossRef]
27. Stjerndahl, M.; Andersson, M.; Hall, H.E.; Pajerowski, D.M.; Meisel, M.W.; Duran, R.S. Superparamagnetic Fe_3O_4/SiO_2 Nanocomposites: Enabling the Tuning of Both the Iron Oxide Load and the Size of the Nanoparticles. *Langmuir* **2008**, *24*, 3532–3536. [CrossRef]
28. Starsich, F.H.L.; Sotiriou, G.A.; Wurnig, M.C.; Eberhardt, C.; Hirt, A.; Boss, A.; Pratsinis, S.E. Silica-Coated Nonstoichiometric Nano Zn-Ferrites for Magnetic Resonance Imaging and Hyperthermia Treatment. *Adv. Health Mater.* **2016**, *5*, 2698–2706. [CrossRef]
29. Ni, X.; Zheng, Z.; Hub, X.; Xiao, X. Silica-coated iron nanocubes: Preparation, characterization, and application in microwave absorption. *J. Colloid Interface Sci.* **2010**, *345*, 234–240. [CrossRef]
30. Zhang, H.; Huang, H.; He, S.; Zeng, H.; Pralle, A. Monodisperse Magnetofluorescent Nanoplatforms for Local Heating and Temperature Sensing. *Nanoscale* **2014**, *6*, 13463–13469. [CrossRef]
31. Lai, C.-W.; Wang, Y.-H.; Lai, C.-H.; Yang, M.-J.; Chen, C.-Y.; Chou, P.-T.; Chan, C.-S.; Chi, Y.; Chen, Y.-C.; Hsiao, J.-K. Iridium-Complex-Functionalized Fe_3O_4/SiO_2 Core/Shell Nanoparticles: A Facile Three-in-One System in Magnetic Resonance Imaging, Luminescence Imaging, and Photodynamic Therapy. *Small* **2008**, *4*, 218–224. [CrossRef]
32. Kacenka, M.; Kaman, O.; Kikerlova, S.; Pavlu, B.; Jirak, Z.; Jirak, D.; Herynek, V.; Cerny, J.; Chaput, F.; Laurent, S.; et al. Fluorescent magnetic nanoparticles for cell labeling: Flux synthesis of manganite particles and novel functionalization of silica shell. *J. Colloid Interface Sci.* **2015**, *447*, 97–106. [CrossRef] [PubMed]

33. Horny, M.-C.; Gamby, J.; Dupuis, V.; Siaugue, J.-M. Magnetic Hyperthermia on γ-Fe_2O_3@SiO_2 Core-Shell Nanoparticles for mi-RNA 122 Detection. *Nanomaterials* **2021**, *11*, 149. [CrossRef]
34. Adams, S.A.; Hauser, J.L.; Allen, A.L.C.; Lindquist, K.P.; Ramirez, A.P.; Oliver, S.; Zhang, J.Z. Fe_3O_4@SiO_2 Nanoparticles Functionalized with Gold and Poly(vinylpyrrolidone) for Bio-Separation and Sensing Applications. *ACS Appl. Nano Mater.* **2018**, *1*, 1406–1412. [CrossRef]
35. Lafuente-Gómez, N.; Milán-Rois, P.; García-Soriano, D.; Luengo, Y.; Cordani, M.; Alarcón-Iniesta, H.; Salas, G.; Somoza, Á. Smart Modification on Magnetic Nanoparticles Dramatically Enhances Their Therapeutic Properties. *Cancers* **2021**, *13*, 4095. [CrossRef]
36. Cano, I.; Martin, C.; Fernandes, J.A.; Lodge, R.W.; Dupont, J.; Casado-Carmona, F.A.; Lucena, R.; Cardenas, S.; Sans, V.; del Pedro, I. Paramagnetic Ionic Liquid-Coated SiO_2@Fe_3O_4 Nanoparticles-The Next Generation of Magnetically Recoverable Nanocatalysts Applied in the Glycolysis of PET. *Appl. Catal. B Environ.* **2020**, *260*, 118110. [CrossRef]
37. Ding, H.L.; Zhang, Y.X.; Wang, S.; Xu, J.M.; Xu, S.C.; Li, G.H. Fe_3O_4@SiO_2 Core/Shell Nanoparticles: The Silica Coating Regulations with a Single Core for Different Core Sizes and Shell Thicknesses. *Chem. Mater.* **2012**, *24*, 4572–4580. [CrossRef]
38. Chen, F.; Bu, W.; Chen, Y.; Fan, Y.; He, Q.; Zhu, M.; Liu, X.; Zhou, L.; Zhang, S.; Peng, W.; et al. A Sub-50-nm Monosized Superparamagnetic Fe_3O_4@SiO_2 T2-Weighted MRI Contrast Agent: Highly Reproducible Synthesis of Uniform Single-Loaded Core–Shell Nanostructures. *Chem. Asian J.* **2009**, *4*, 1809–1816. [CrossRef]
39. Vestal, C.R.; Zhang, Z.J. Synthesis and Magnetic Characterization of Mn and Co Spinel Ferrite-Silica Nanoparticles with Tunable Magnetic Core. *Nano Lett.* **2003**, *3*, 1739–1743. [CrossRef]
40. Tago, T.; Hatsuta, T.; Miyajima, K.; Kishida, M.; Tashiro, S.; Wakabayashi, K. Novel Synthesis of Silica-Coated Ferrite Nanoparticles Prepared Using Water-in-Oil Microemulsion. *J. Am. Ceram. Soc.* **2002**, *85*, 2188–2194. [CrossRef]
41. Iacovita, C.; Fizeșan, I.; Nitica, S.; Florea, A.; Barbu-Tudoran, L.; Dudric, R.; Pop, A.; Vedeanu, N.; Crisan, O.; Tetean, R.; et al. Silica Coating of Ferromagnetic Iron Oxide Magnetic Nanoparticles Significantly Enhances Their Hyperthermia Performances for Efficiently Inducing Cancer Cells Death In Vitro. *Pharmaceutics* **2021**, *13*, 2026. [CrossRef]
42. Lu, Y.; Yin, Y.; Mayers, B.T.; Xia, Y. Modifying the Surface Properties of Superparamagnetic Iron Oxide Nanoparticles through A Sol-Gel Approach. *Nano Lett.* **2002**, *2*, 183–186. [CrossRef]
43. Kolhatkar, A.G.; Nekrashevich, I.; Litvinov, D.; Willson, R.C.; Lee, T.R. Cubic Silica-Coated and Amine-Functionalized FeCo Nanoparticles with High Saturation Magnetization. *Chem. Mater.* **2013**, *25*, 1092–1097. [CrossRef] [PubMed]
44. Pinho, S.L.C.; Laurent, S.; Roch, J.A.; Delville, M.-H.; Mornet, S.; Carlos, L.D.; Elst, L.V.; Muller, R.N.; Geraldes, C.F.G.C. Relaxometric Studies of γ-Fe_2O_3@SiO_2 Core-Shell Nanoparticles: When the Coating Matters. *J. Phys. Chem. C* **2012**, *116*, 2285–2291. [CrossRef]
45. Noh, S.-y.; Na, W.; Jang, J.-t.; Lee, J.-H.; Lee, E.-J.; Moon, S.-H.; Lim, Y.; Shin, J.-S.; Cheon, J. Nanoscale Magnetism Control via Surface and Exchange Anisotropy for Optimized Ferrimagnetic Hysteresis. *Nano Lett.* **2012**, *12*, 3716–3721. [CrossRef] [PubMed]
46. Ait Kerroum, M.A.; Iacovita, C.; Baaziz, W.; Ihiawakrim, D.; Rogez, G.; Benaissa, M.; Lucaciu, C.M.; Ersen, O. Quantitative Analysis of the Specific Absorption Rate Dependence on the Magnetic Field Strength in $Zn_xFe_{3-x}O_4$ Nanoparticles. *Int. J. Mol. Sci.* **2020**, *21*, 7775. [CrossRef]
47. Iacovita, C.; Florea, A.; Scorus, L.; Pall, E.; Dudric, R.; Moldovan, A.I.; Stiufiuc, R.; Tetean, R.; Lucaciu, C.M. Hyperthermia, Cytotoxicity, and Cellular Uptake Properties of Manganese and Zinc Ferrite Magnetic Nanoparticles Synthesized by a Polyol-Mediated Process. *Nanomaterials* **2019**, *9*, 1489. [CrossRef]
48. Baaziz, W.; Pichon, B.P.; Fleutot, S.; Liu, Y.; Lefevre, C.; Grenache, J.M.; Toumi, M.; Mhiri, T.; Begin-Colin, S. Magnetic Iron Oxide Nanoparticles: Reproducible Tuning of the Size and Nanosized-Dependent Composition, Defects, and Spin Canting. *J. Phys. Chem. C* **2014**, *118*, 3795–3810. [CrossRef]
49. Wang, M.; Peng, M.-L.; Cheng, W.; Cui, Y.-L.; Chen, C. A Novel Approach for Transferring Oleic Acid Capped Iron Oxide Nanoparticles to Water Phase. *J. Nanosci. Nanotechnol.* **2011**, *11*, 3688–3691. [CrossRef]
50. Abbas, M.; Torati, S.R.; Kim, C.G. A novel approach for the synthesis of ultrathin silica-coated iron oxide nanocubes decorated with silver nanodots (Fe_3O_4/SiO_2/Ag) and their superior catalytic reductio of 4-nitroaniline. *Nanoscale* **2015**, *7*, 12192–12204. [CrossRef]
51. Morales, I.; Costo, R.; Mille, N.; Carrey, J.; Hernando, A.; de la Presa, P. Time-dependent AC magnetometry and chain formation in magnetite: The influence of particle size, initial temperature and the shortening of the relaxation time by the applied field. *Nanoscale Adv.* **2021**, *3*, 5801–5812. [CrossRef]
52. Gandia, D.; Gandarias, L.; Rodrigo, I.; Robles-Garcia, J.; Das, R.; Garaio, E.; Angel Garcia, J.; Phan, M.-H.; Srikanth, H.; Orue, I.; et al. Unlocking the Potential of Magnetotactic Bacteria as Magnetic Hyperthermia Agents. *Small* **2009**, *15*, 1902626. [CrossRef] [PubMed]
53. Materia, M.E.; Guardia, P.; Sathya, A.; Leal, M.P.; Marotta, R.; Di Corato, R.; Pellegrino, T. Mesoscale assemblies of iron oxide nanocubes as heat mediators and image contrast agents. *Langmuir* **2015**, *31*, 808–816. [CrossRef] [PubMed]
54. Branquinho, L.C.; Carriao, M.S.; Costa, S.A.; Zufelato, N.; Sousa, M.; Miotto, R.; Ivkov, R.; Bazukis, A.F. Effect of magnetic dipolar interactions on nanoparticles heating efficiency: Implications for cancer hyperthermia. *Sci. Rep.* **2014**, *3*, 2887. [CrossRef]
55. Martinez-Boubeta, C.; Simeonidis, K.; Makridis, A.; Angelakeris, M.; Ilesias, O.; Guardia, P.; Cabot, A.; Yedra, L.; Estrade, S.; Peiro, F.; et al. Learning from nature to improve the heat generation of iron-oxide nanoparticles for magnetic hyperthermia applications. *Sci. Rep.* **2013**, *3*, 1652. [CrossRef]

56. Iacovita, C.; Stiufiuc, R.; Radu, T.; Florea, A.; Stiufiuc, G.; Dutu, A.; Mican, S.; Tetean, R.; Lucaciu, C.M. Polyethylene Glycol-Mediated Synthesis of Cubic Iron Oxide Nanoparticles with High Heating Power. *Nanoscale Res. Lett.* **2015**, *10*, 391. [CrossRef]
57. Deatsch, A.E.; Evans, B.A. Heating efficiency in magnetic hyperthermia. *J. Mag. Mag. Mat.* **2014**, *354*, 163–172. [CrossRef]
58. Blanco-Andujar, C.; Ortega, D.; Southern, P.; Pankhurst, Q.A.; Thanh, N.T.K. High performance multi-core iron oxide nanoparticles for magnetic hyperthermia: Microwave assisted synthesis and the role of core-to-core interactions. *Nanoscale* **2015**, *7*, 1768–1775. [CrossRef]
59. Iacovita, C.; Fizeșan, I.; Pop, A.; Scorus, L.; Dudric, R.; Stiufiuc, G.; Vedeanu, N.; Tetean, R.; Loghin, F.; Stiufiuc, R.; et al. In Vitro Intracellular Hyperthermia of Iron Oxide Magnetic Nanoparticles, Synthesized at High Temperature by a Polyol Process. *Pharmaceutics* **2020**, *12*, 424. [CrossRef]
60. Yu, X.; Wang, L.; Li, K.; Mi, Y.; Li, Z.; Wu, D.; Sun, F.; He, S.; Zeng, H. Tuning dipolar effects on magnetic hyperthermia of $Zn_{0.3}Fe_{2.7}O_4/SiO_2$ nanoparticles by silica shell. *J. Mag. Mag. Mat.* **2021**, *521*, 167483. [CrossRef]
61. Sanz, B.; Calatayud, M.P.; De Biasi, E.; Lima Jr., E.; Mansilla, M.V.; Zysler, R.D.; Ibarra, M.R.; Goya, G.F. In Silico before In Vivo: How to Predict the Heating Efficiency of Magnetic Nanoparticles within the Intracellular Space. *Sci. Rep.* **2016**, *6*, 38733. [CrossRef] [PubMed]
62. Reczynska, K.; Marszalek, M.; Zarzycki, A.; Reczynski, W.; Kornaus, K.; Pamula, E.; Chrzanowski, W. Superparamagnetic Iron Oxide Nanoparticles Modified with Silica Layers as Potential Agents for Lung Cancer Treatment. *Nanomaterials* **2020**, *10*, 1076. [CrossRef] [PubMed]
63. Yameen, B.; Choi, W.I.; Vilos, C.; Swami, A.; Shi, J.; Farokhzad, O.C. Insight into nanoparticle cellular uptake and intracellular targeting. *J. Control. Release* **2014**, *190*, 485–499. [CrossRef] [PubMed]
64. He, Y.; Qin, J.; Wu, S.; Yang, H.; Wen, H.; Wang, Y. Cancer cell–nanomaterial interface: Role of geometry and surface charge of nanocomposites in the capture efficiency and cell viability. *Biomater. Sci.* **2019**, *7*, 2759–2768. [CrossRef] [PubMed]
65. Schweiger, C.; Hartman, R.; Zhang, F.; Parak, W.J.; Kissel, T.H.; Gil, P.R. Quantification of the internalization patterns of superparamagnetic iron oxide nanoparticles with opposite charge. *J. Nanobiotechnol.* **2012**, *10*, 28. [CrossRef]
66. Calero, M.; Gutierrez, L.; Salas, G.; Luengo, Y.; Lazaro, A.; Acedo, P.; Morales, M.P.; Miranda, R.; Villanueva, A. Efficient and safe internalization of magnetic iron oxide nanoparticles: Two fundamental requirements for biomedical applications. *Nanomed. Nanotechnol. Biol. Med.* **2014**, *10*, 733–743. [CrossRef]
67. Fizesan, I.; Iacovita, C.; Pop, A.; Kiss, B.; Dudric, R.; Stiufiuc, R.; Lucaciu, C.M.; Loghin, F. The Effect of Zn-Substitution on the Morphological, Magnetic, Cytotoxic, and In Vitro Hyperthermia Properties of Polyhedral Ferrite Magnetic Nanoparticles. *Pharmaceutics* **2021**, *13*, 2148. [CrossRef]
68. Gavard, J.; Hanini, A.; Schmitt, A.; Kacem, K.; Chau, F.; Ammar, S. Evaluation of iron oxide nanoparticle biocompatibility. *Int. J. Nanomed.* **2011**, *6*, 787–794. [CrossRef]
69. Ong, K.J.; MacCormack, T.J.; Clark, R.J.; Ede, J.D.; Ortega, V.A.; Felix, L.C.; Dang, M.K.M.; Ma, G.; Fenniri, H.; Veinot, J.G.C.; et al. Widespread nanoparticle-assay interference: Implications for nanotoxicity testing. *PLoS ONE* **2014**, *9*, e90650. [CrossRef]
70. Konczol, M.; Ebeling, S.; Goldenberg, E.; Treude, F.; Gminski, R.; Giere, R.; Grobety, B.; Rothen-Rutishauser, B.; Merfor, I.; Mersch-Sundermann, V. Cytotoxicity and genotoxicity of size-fractionated iron oxide (magnetite) in A549 human lung epithelial cells: Role of ROS, JNK, and NF-κB. *Chem. Res. Toxicol.* **2011**, *24*, 1460–1475. [CrossRef]
71. Feng, Y.; Tinsley Oden, J.; Rylander, M.N. A two-state cell damage model under hyperthermic conditions: Theory and in vitro experiments. *J. Biomech. Eng.* **2008**, *130*, 041016. [CrossRef] [PubMed]